Wintertime Nonbrightband Rain in California and Oregon during CALJET and PACJET: Geographic, Interannual, and Synoptic Variability

PAUL J. NEIMAN, GARY A. WICK, AND F. MARTIN RALPH
NOAA/Environmental Technology Laboratory, Boulder, Colorado

BROOKS E. MARTNER, ALLEN B. WHITE, AND DAVID E. KINGSMILL
NOAA/Environmental Technology Laboratory, and Cooperative Institute for Research in Environmental Sciences, University of Colorado, Boulder, Colorado

(Manuscript received 16 July 2004, in final form 19 October 2004)

ABSTRACT

An objective algorithm presented in White et al. was applied to vertically pointing S-band (S-PROF) radar data recorded at four sites in northern California and western Oregon during four winters to assess the geographic, interannual, and synoptic variability of stratiform nonbrightband (NBB) rain in landfalling winter storms. NBB rain typically fell in a shallow layer residing beneath the melting level (<~3.5 km MSL), whereas rainfall possessing a brightband (BB) was usually associated with deeper echoes (>~6 km MSL). The shallow NBB echo tops often resided beneath the coverage of the operational Weather Surveillance Radar-1988 Doppler (WSR-88D) scanning radars yet were still capable of producing flooding rains.

NBB rain contributed significantly to the total winter-season rainfall at each of the four geographically distinct sites (i.e., 18%–35% of the winter-season rain totals). In addition, the rainfall observed at the coastal mountain site near Cazadero, California (CZD), during each of four winters was composed of a significant percentage of NBB rain (18%–50%); substantial NBB rainfall occurred regardless of the phase of the El Niño–Southern Oscillation (which ranged from strong El Niño to moderate La Niña conditions). Clearly, NBB rain occurs more widely and commonly in California and Oregon than can be inferred from the single-winter, single-site study of White et al.

Composite NCEP–NCAR reanalysis maps and Geostationary Operational Environment Satellite (GOES) cloud-top temperature data were examined to evaluate the synoptic conditions that characterize periods of NBB precipitation observed at CZD and how they differ from periods with bright bands. The composites indicate that both rain types were tied generally to landfalling polar-cold-frontal systems. However, synoptic conditions favoring BB rain exhibited notable distinctions from those characterizing NBB periods. This included key differences in the position of the composite 300-mb jet stream and underlying cold front with respect to CZD, as well as notable differences in the intensity of the 500-mb shortwave trough offshore of CZD. The suite of BB composites exhibited dynamically consistent synoptic-scale characteristics that yielded stronger and deeper ascent over CZD than for the typically shallower NBB rain, consistent with the GOES satellite composites that showed 20-K warmer (2.3-km shallower) cloud tops for NBB rain. Composite soundings for both rain types possessed low-level potential instability, but the NBB sounding was warmer and moister with stronger low-level upslope flow, thus implying that orographically forced rainfall is enhanced during NBB conditions.

1. Introduction

Winter storm forecasting for the West Coast of the United States is handicapped by a combination of sparse upstream observations and the complicated orographic enhancement of precipitation, given that long, unobstructed fetches of very moist airflow encounter the abrupt terrain of coastal mountain ranges. The moisture is often tightly concentrated into narrow corridors or "atmospheric rivers" across the Pacific Ocean by potent storms that produce floods, wind damage, and storm-related injuries and fatalities upon landfall (Ralph et al. 2004). The California Land-falling Jets Experiment [CALJET; see related studies by Neiman et al. (2002, 2004); Ralph et al. (2003)] of the winter of 1997/98 and the Pacific Land-Falling Jets Experiment (PACJET; White et al. 2002) in the winters of 2000/01, 2001/02, and 2002/03 were designed to investigate these factors, with the long-term goal of improving forecasts,

---

Corresponding author address: Paul J. Neiman, NOAA/Environmental Technology, Laboratory Mail Code R/ET7, 325 Broadway, Boulder, CO 80305.
Email: Paul.J.Neiman@noaa.gov

especially in California. Related programs focused farther north in Washington and Oregon include the Cyclonic Extratropical Storms Project (CYCLES; Matejka et al. 1980), the Coastal Observation and Simulation with Topography Experiment (COAST; Bond et al. 1997), and the Improvement of Microphysical Parameterization through Observations and Verification Experiment (IMPROVE; Stoelinga et al. 2003).

The CALJET and PACJET field experiments took place in a variety of El Niño–Southern Oscillation (ENSO) winter-season conditions, including the very strong El Niño of 1997/98 and the moderate La Niña of 2000/01. The experiments highlighted the use of ground-based radar profiling systems, including vertically pointing S-Band (2875 MHz) precipitation profilers and 915-MHz wind profilers from the National Oceanic and Atmospheric Administration's Environmental Technology Laboratory (NOAA/ETL). These upward pointing Doppler radars monitored conditions aloft at coastline, mountain, and valley locations. Instrument siting (see Fig. 1; Table 1) emphasized California's coastal regions, but also included sites farther inland in the foothills of California's Sierra Nevada (Grass Valley—GVY) and Oregon's Cascades Range (McKenzie Bridge—MBO). Each of the four winter experiments included an S-band precipitation profiler (hereafter, S-PROF) and rain gauge system located in the coastal mountains at 475 m above mean sea level (MSL) near the town of Cazadero (CZD) about 120 km northwest of San Francisco.

White et al. (2003) examined bulk microphysical aspects of the orographic rainfall process using data collected with the S-PROF radar at CZD during the CALJET winter of 1997/98. They documented the common occurrence and discussed the practical ramifications of shallow orographically enhanced precipitation in this area. Their analyses revealed that a large fraction (28%) of that winter's rain fell during periods when the storm clouds produced no detectable melting-layer radar bright band. These periods were objectively classified as nonbrightband (NBB) precipitation, in contrast to more common situations in which a radar brightband (BB precipitation) was evident. The brightband is indicative of hydrometeor growth dominated by ice processes (e.g., Battan 1973; Fabry and Zawadzki 1995), whereas its absence suggests strongly that ice plays a secondary role to the collision-coalescence process (Cotton and Anthes 1989; Zipser and LeMone 1980). White et al. (2003) showed that the NBB radar echoes were usually shallow, often not reaching the freezing level or extending only modestly above it, and they were nonconvective. These echoes were associated with stronger orographic forcing than the BB echoes [consistent with numerical modeling results by Young (1974) and Song and Marwitz (1989)], as revealed by collocated wind-profiler measurements of the upslope component of the flow in the boundary layer. The season-averaged rainfall rates were nearly the same (~4 mm h^{-1}) for the NBB and BB categories. Rain rates as high as 20 mm h^{-1} were recorded during NBB periods, which exceeds the rule-of-thumb rain-rate threshold of 12 mm h^{-1} used by local forecasters for guidance in issuing flood statements. The S-PROF data from the CALJET winter indicated that durations of NBB and BB periods were quite variable, with both kinds of precipitation often occurring in the same storm. Similarly, aircraft radar data presented by White et al. (2003) show that the presence or absence of the bright band varied over horizontal scales of only a few tens of kilometers. Nevertheless, some storms were dominated by either BB or NBB rainfall, as will be shown more

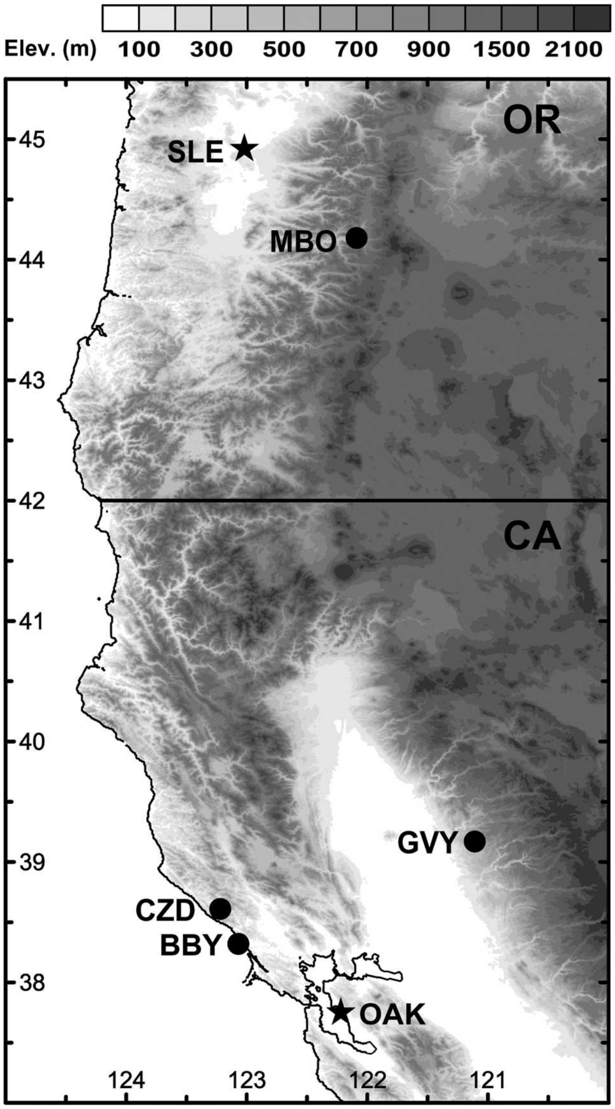

FIG. 1. Terrain base map of northern California and southern Oregon showing the locations of the four vertically pointing S-band (i.e., S-PROF) radar profiler sites (bold black dots) at Cazadero (CZD), Bodega Bay (BBY), Grass Valley (GVY), and McKenzie Bridge (MBO), and two rawinsonde sounding sites (black stars) at Oakland (OAK) and Salem (SLE).

Table 1. Site information, operating periods, and operating modes for the vertically pointing S-band (i.e., S-PROF) radars used in this study. The last column indicates whether or not a 915-MHz wind profiler operated alongside the S-PROF radars.

									Combined mode		
Location	Station name	Lat (°N)	Lon (°W)	Elev (m)	Experiment name	Start date	End date	Mode types*	Frequency (h^{-1})	Vertical resolution (m)	Wind profiler
Cazadero, CA	CZD	38.61	123.21	475	CALJET	1 Jan 1998	31 Mar 1998	1, 2 , 3	34	105	Yes
Cazadero, CA	CZD	38.61	123.21	475	PACJET-2001	12 Jan 2001	8 Mar 2001	1, 3	89	60	No
Cazadero, CA	CZD	38.61	123.21	475	PACJET-2002	16 Dec 2001	6 Apr 2002	1, 3	89	60	No
Cazadero, CA	CZD	38.61	123.21	475	PACJET-2003	9 Dec 2002	9 Apr 2003	1, 2, 3	100	60	No
Bodega Bay, CA	BBY	38.31	123.07	12	PACJET-2001	12 Jan 2001	8 Mar 2001	1, 2, 3	72	60	Yes
Grass Valley, CA	GVY	39.17	121.11	689	PACJET-2002	17 Jan 2002	8 Apr 2002	1, 3	89	60	Yes
McKenzie Bridge, OR	MBO	44.18	122.09	512	IMPROVE	15 Nov 2001	13 Jan 2002	1, 2	120**	105**	Yes

* The S-PROF modes are as follows: 1 = heavy precipitation; 2 = light precipitation; 3 = clouds.

** Only mode 2 was used in this study. Mode 1 was available, but with 45-m vertical resolution.

clearly in the present study, which expands on the earlier work.

The season-averaged S-PROF measurements of the rainfall aloft at CZD showed that the NBB precipitation had radar reflectivities that were 8 dBZ less, and downward mean vertical Doppler velocities of 4 m s^{-1} less, than corresponding BB precipitation in the CALJET winter (White et al. 2003). Yet, both NBB and BB periods produced nearly the same average rainfall rate recorded by the collocated rain gauge. This evidence strongly indicates that the NBB rainfall is composed of unusually high concentrations of small drops and few or no large drops. In this respect, the rain is similar to that in orographic clouds in Hawaii (Blanchard 1953), although the presence of small ice crystals in upper parts of the California clouds cannot be ruled out. Because of the uncommon drop size distribution, the reflectivity–rainfall (Z–R) relationship used operationally by the network of Weather Surveillance Radar-1988 Doppler units (WSR-88Ds) significantly underestimates rain intensities and accumulations in these situations. Often, these radars do not even detect the NBB precipitation at all, because their lowest sweeps pass over the shallow echo tops in this area, or are blocked by intervening mountains (White et al. 2003). This radar coverage problem is common throughout the West (Westrick et al. 1999; Maddox et al. 2002). The apparently unusual drop size distributions in NBB precipitation also have implications for the accuracy of rainfall retrievals from spaceborne precipitation radars, such as that of the Tropical Rainfall Measurement Mission (TRMM; Kummerow et al. 2000) satellite and its anticipated successor, the Global Precipitation Measurement (GPM) core satellite.

For these reasons, it is crucial to determine whether the earlier results reported by White et al. (2003) for a single winter at one location are representative of other winters and areas, or, if they are uncommon and perhaps associated only with strong El Niño seasons. From a forecasting and nowcasting perspective, it is also important to assess synoptic regimes and phases of ENSO that may favor NBB or BB rain, which is possible to accomplish with the multiwinter dataset. In particular, because NBB rainfall is quite likely underestimated by ground- and space-based remote sensing systems, forecasters should be aware of specific linkages between synoptic and ENSO conditions and rain type. The present article addresses these issues by significantly extending the work of White et al. (2003), which served largely to identify NBB rain at a midlatitude coastal mountain site. Specifically, this new study examines similar S-PROF datasets from CZD for all four CALJET–PACJET winters and for three additional sites, BBY, GVY, and MBO. Interannual and geographic variations of the BB and NBB rain types defined in the earlier work are determined. In addition, the present article investigates the sensitivity of rain type to the ENSO cycle and examines the synoptic-scale meteorological conditions that favor the development of BB versus NBB rain at CZD.

2. Observing systems

During the CALJET and three PACJET winters, numerous research observing platforms were deployed across the West Coast of the United States, and they complemented the existing operational observing networks. Those observing systems that are critical to this study are described briefly in the following paragraphs.

A NOAA/ETL S-PROF precipitation profiler (λ = 10 cm; f = 2875 MHz) with extended dynamic range (White et al. 2000) gathered data in California's coastal mountains at CZD during each of the four winter experiments (Fig. 1; Table 1). NOAA/ETL carried out additional, single-winter, S-PROF deployments along the California coast at BBY between January and March 2001 during PACJET-2001, in the Sierra Nevada foothills at GVY between January and April 2002 during PACJET-2002, and in Oregon's Cascades at MBO between November 2001 and January 2002 during IMPROVE (Fig. 1; Table 1). Each S-PROF site was equipped with a tipping-bucket rain gauge and a 10-m surface meteorological tower. The rain gauges measured rainfall with 0.01-in. (~0.25 mm) resolution every 2 min, except every 1 min at CZD and BBY during PACJET-2001. The tower-borne instrumentation recorded temperature, moisture, pressure, and wind velocity with the same temporal resolution as the rain gauges. A 915-MHz wind profiler (Carter et al. 1995) accompanied each S-PROF radar, except at CZD during the PACJET winters (Table 1). These wind profilers routinely provided hourly averaged profiles of horizontal wind velocity from 0.1 to 4.0 km above ground with ≤100 m vertical resolution in clear, cloudy, and precipitating conditions.

The vertically pointing S-PROF radars were programmed with slightly different operating modes (see Table 1), depending partly on the specific science objectives associated with each deployment. For a detailed explanation of these modes and the postprocessing methods, see White et al. (2000). The radar cycled through two or three modes, and the data from these individual modes were combined in postprocessing into a single, combined mode. Although the temporal and vertical resolutions of the individual modes were not identical at all sites and in all winters, the combined-mode processing was designed to minimize the differences.

Two operational observing networks also yielded data vital to this study. Operational and supplemental rawinsondes at Oakland, California, and Salem, Oregon (OAK and SLE, respectively, in Fig. 1) provided ≤12 h resolution thermodynamic and wind sampling of the troposphere, including accurate measurements of the height of the melting level (i.e., the 0°C level), which are presented in section 3b. Three Geostationary Operational Environmental Satellites (i.e., *GOES-8*, *-9*, and *-10*) furnished 3-h resolution infrared (IR) data that were used to create a unique pair of composite satellite images shown in section 4b(2).

3. S-PROF observations in California and Oregon

a. Process partitioning of rainfall

The rainfall process-partitioning algorithm developed by White et al. (2003) was applied to the S-PROF combined-mode profiles to provide an initial objective estimate of the occurrence and total accumulation of BB and NBB rain that fell at each site. Analysis was performed on all half-hour periods when the rain rate exceeded ~1 mm h^{-1} (i.e., two rain gauge tips per half hour). If the percentage of profiles containing a BB in the half hour met or exceeded 50%, the rainfall was ascribed to BB rain. Otherwise, the NBB rain process was designated. The objective algorithm takes advantage of the fact that BB rain is formed through ice crystal growth and subsequent melting, and that melting hydrometeors beneath the BB (which, in turn, is ~100–300 m below the 0°C level) yield larger downward Doppler vertical velocities (DVVs) than the less dense ice crystals aloft (e.g., Battan 1973; Anagnostou and Kummerow 1997). Beneath the BB, the reflectivity and DVV fields remain relatively constant with decreasing altitude. In contrast, NBB rain, by definition, does not possess a BB and often forms in a shallow layer beneath the melting level. The reflectivity and DVV fields both increase steadily with decreasing height, likely due to collision coalescence (White et al. 2003).[1]

A bright band is also usually absent in convective precipitation because of enhanced turbulence, or the presence of hail or graupel, flanking the melting level. As a result, the objective algorithm typically tagged convection as NBB rain. Therefore, we visually inspected the S-PROF data collected during each half-hour period ascribed to NBB rain in conjunction with perusal of collocated (and/or nearby) wind-profiler and surface data to subjectively evaluate whether or not the rain was associated with convection (as in White et al. 2003). This subjective step proved beneficial and yielded three distinct rainfall types: BB, NBB, and convective.

Occasionally, when the bright band resided beneath the minimum detectable range of the radar or when wet snow reached the surface and melted in the rain gauge, the objective algorithm erroneously characterized the rain as NBB. These situations were easily diagnosed by the concurrent visual inspection of the collocated S-PROF and surface data, and the relevant half-hour time periods were subsequently categorized as "missing." The objective algorithm successfully tagged half-hour periods as "missing" for two additional scenarios related to snow, that is, when at least 1 mm of rainfall was recorded but the minimum reflectivity threshold of 10 dBZ_e in the lowest range gate (see White et al. 2003) was not met. This occurred when previously accumulated snow melted into the rain gauge during nonprecipitating conditions or when wet snow on the S-PROF antenna severely attenuated the radar beam during precipitating conditions.

b. Representative NBB rain events

In an effort to highlight the distinctly different character of BB and NBB rain in the S-PROF data and to

---

[1] White et al. (2003) documented a hybrid rain type with both BB and NBB attributes. Roughly three-quarters of the BB rainfall during CALJET was associated with hybrid conditions, which quite likely results when ice provides seeding from aloft and grows in liquid phase beneath the BB via the collision-coalescence process. However, we chose to differentiate only between BB and NBB rain and the synoptic conditions associated with them, because NBB rainfall is often poorly observed by the operational radar network and satellite-based retrievals.

show common attributes of NBB rain at different geographic regions, we present illustrative radar observations of NBB-dominated rain events from CZD, GVY, and MBO. Each event encompassed 14 h of S-PROF data extending up to 8.5 km MSL. Time–height sections of radar reflectivity and DVV from CZD (Fig. 2) show an intermittent mix of BB and NBB rain between 1400 and 1600 UTC 23 March 1998 during the period when uncoupled upper and lower reflectivity layers were initially merging ahead of an approaching cold front (a detailed analysis of this storm is presented in White et al. 2003). The front itself was accompanied by a convective narrow cold-frontal rainband (NCFR) between 1600 and 1630 UTC followed by a 60-min period of stratiform rain characterized by a prominent bright band, a large vertical gradient of DVV at ~2.3 km MSL, and deep echoes extending to 8 km MSL. Thereafter, shallow NBB rain commenced and persisted for 6 h, during which the upper reflectivity layer decoupled and eventually disappeared by 1930 UTC. The postfrontal NBB rain was initially heavy (9–18 mm h^{-1}) but eventually diminished considerably in intensity (<5 mm h^{-1}). During this storm, the radar bright band resided several hundred meters beneath the 0°C level observed by the closest rawinsondes, and the strongest reflectivities and DVVs during the NBB rain were also confined well beneath the melting level. Of the ~75 mm of rain that fell at CZD, >62 mm fell without a bright band, thus revealing that NBB rain can contribute significantly to the rainfall totals of storms that affect California's coastal mountains.

Figure 3 portrays S-PROF observations of an NBB rain event at GVY between 0000 and 1400 UTC 20 February 2002. Synoptic charts and collocated wind-profiler data (not shown) reveal that this event was characterized by an extended period of weak warm advection through a deep layer of the troposphere in the absence of an extratropical cyclone (not shown). The initial hour shows shallow NBB rain and intermittent enhanced echoes aloft. During the next 2.5 h, a bright band and vertical DVV gradient were observed at ~2.5 km MSL, that is, several hundred meters beneath the rawinsonde-observed 0°C level. Deep echoes extending upward to ~6 km MSL coincided with the period of BB rain. An intermittent brightband signature dissipated within NBB conditions between 0330 and 0430 UTC during a steady decrease in the echo depth. Thereafter, steady but mostly light NBB rain persisted in a shallow

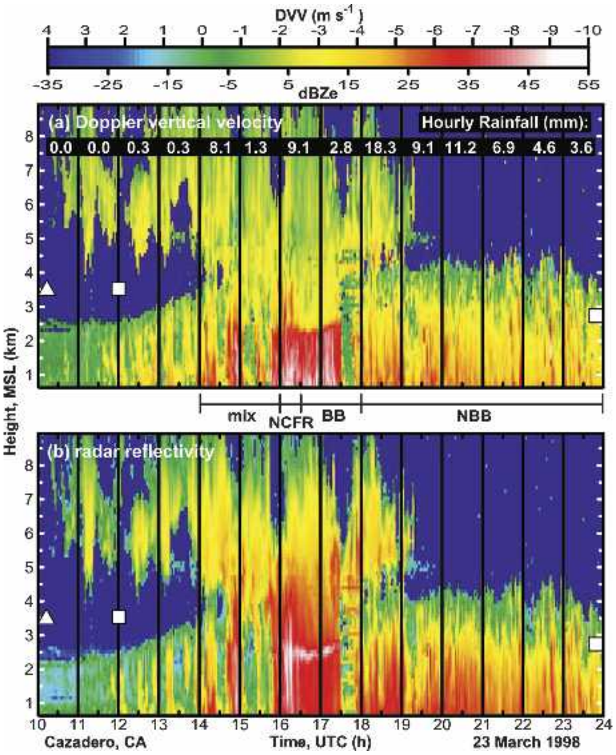

FIG. 2. Time–height sections of (a) DVV (m s^{-1}) and (b) equivalent radar reflectivity factor (dBZ_e), recorded by the S-PROF radar at Cazadero, CA, for the period 1000 UTC 23 Mar to 0000 UTC 24 Mar 1998. The hourly rainfall accumulations (mm) measured by a tipping-bucket rain gauge collocated with the radar are listed in (a). The 0°C altitudes are measured by Oakland, CA, rawinsondes (bold white squares are direct measurements, and bold white triangles are temporally interpolated measurements from adjacent launches). The dominant rainfall types (BB = brightband rain, NBB = nonbrightband rain, mix = intermittent BB and NBB rain, NCFR = narrow cold-frontal rainband) are labeled between (a) and (b).

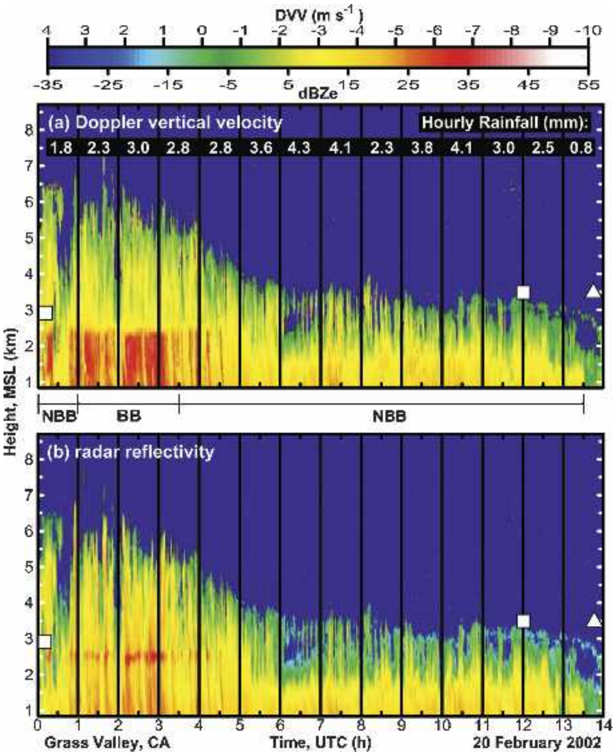

FIG. 3. The same as in Fig. 2, except for Grass Valley, CA, for the period 0000 to 1400 UTC 20 Feb 2002.

layer well beneath the melting level at 3.5 km MSL. The NBB rain event at MBO between 0800 and 2200 UTC 13 December 2001 (Fig. 4) also occurred during deep-tropospheric warm advection, but ahead of an approaching occluded cyclone. Steady, light NBB rain fell mostly in a shallow layer beneath the 0°C level (2.0–2.3 km MSL) during the first 11.5 h. Within this period, however, there were embedded pulsations of deeper reflectivities (up to ~4 km MSL) possessing intermittent brightband attributes, especially in DVV. After 1930 UTC, a descending bright band was observed within 6.5-km-deep echoes during a cold-frontal passage. Although the NBB rain at both sites was not as intense as at CZD, it was also prolonged and accounted for 34 of the 41 mm of total rainfall at GVY and 23 of 33 mm at MBO.

c. *Winter-season rain-type variability*

The case studies demonstrate that individual rainstorms from three disparate geographic locations can be dominated by NBB rain. However, does NBB rain contribute significantly to the total winter-season rainfall observed at these sites (as well as at BBY on the coast)? To answer this question, the rainfall process-partitioning methodology was applied to the winter-season S-PROF observations recorded at each of the four sites, and the results are presented in Table 2 and Fig. 5.

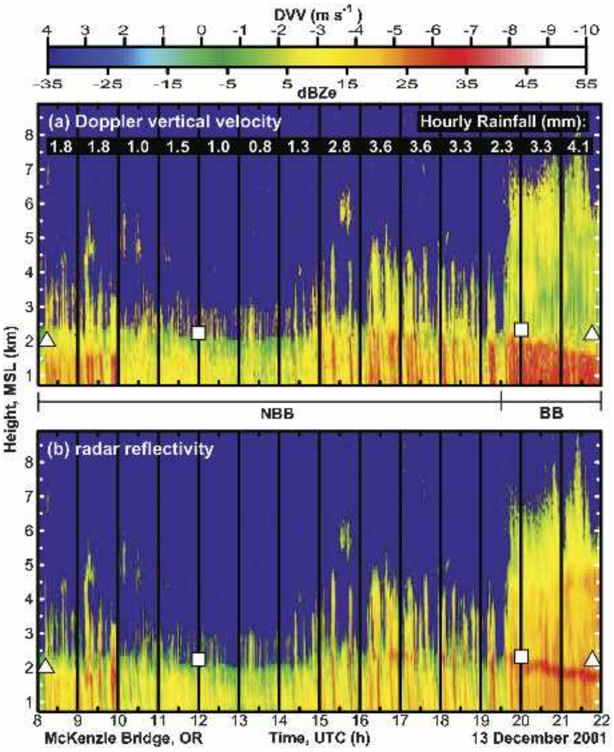

FIG. 4. The same as in Fig. 2, except for McKenzie Bridge, OR, for the period 0800 to 2200 UTC 13 Dec 2001. The 0°C altitudes are measured by Salem, OR, rawinsondes.

A comparison of the total winter-season rainfall observed at these sites (Table 2) reveals that the rainiest winters generally occurred in the coastal mountains at CZD, based on the winter-season totals and on the average rainfall per day. In addition, the largest quantities of both NBB and BB rain fell at CZD. Brightband rain accounted for a majority of the total winter-season rainfall at each of the four sites (Fig. 5a), ranging from ~59% of the total ascribed rainfall at CZD to nearly 82% at MBO. These results imply that deep clouds produced most of the winter-season rainfall at these sites. It should be noted, however, that direct comparisons between sites should be viewed with caution since they involve different winters.

Despite the predominance of BB rain, a significant minority of the total winter-season rainfall occurred without a bright band (Fig. 5b). Specifically, ~18% of the ascribed rainfall at MBO was attributed to NBB conditions. This fractional value jumped to nearly one-quarter at BBY and to ~35% at GVY and CZD. These observations demonstrate unambiguously that shallow NBB rain contributed substantively to the winter-season rainfall at all of these disparate sites and not just at the CZD site examined earlier by White et al. (2003). In contrast, only a small percentage of convective rain fell at these sites (Fig. 5c), primarily at or near the coast (6% at CZD, 8.5% at BBY). Finally, snow-related issues resulted in a small fraction of missing data (Fig. 5d), mainly at the northernmost mountain site at MBO.

4. Multiwinter S-PROF observations at Cazadero, California

The CZD process-partitioning results in Fig. 5 represent an average based on four winters of rainfall observations. In this section, these data are examined in more detail to assess interannual rain-type variability and to determine the mean synoptic-scale conditions responsible for significant rain events at CZD during each of these winters. These data are then stratified by rain type in an effort to explore and contrast the mean synoptic conditions associated with NBB and BB rain.

a. *Interannual rain-type variability and synoptic-scale environments*

The interannual rain-type variability at CZD is shown in Figs. 6a–d and will be discussed in the context of the ENSO phase (Fig. 6e), which is quantified by the multivariate ENSO index (MEI; Wolter and Timlin 1993, 1998). The MEI was a near-record 2.72 during CALJET, thus signifying the presence of a strong warm-phase event referred to as El Niño. The MEI during PACJET-2001 was −0.58, reflecting modest cold-phase or La Niña conditions. Neutral ENSO conditions prevailed during PACJET-2002, while PACJET-2003 was characterized by modest El Niño

TABLE 2. Number of operating days for each S-PROF radar, and the total rainfall, average daily rainfall, and ascribed rainfall (mm) at each of the S-PROF sites. Rainfall is only ascribed to a particular rain type when at least two tips of the rain gauge bucket occur in each half-hour period. The "missing rain" column refers to rainfall that met the two-tip criterion but could not be ascribed to a specific rain type by the objective process-partitioning algorithm because of issues related to snow (see text).

Location and year	No. of operating days	Total (mm)	Average rainfall per day (mm)	NBB rainfall (mm)	BB rainfall (mm)	Convective rainfall (mm)	Missing rain (mm)
CZD-98	90	1841.2	20.5	513.0	1097.0	133.0	35.1
CZD-01	56	662.9	11.8	101.6	415.0	41.4	69.9
BBY-01	56	284.5	5.1	63.2	173.0	22.1	0.0
MBO-01/02	60	617.2	10.3	74.2	341.2	1.8	124.7
CZD-01/02	112	748.8	6.7	339.4	307.8	31.5	4.8
GVY-02	82	321.6	3.9	105.4	191.2	2.3	8.1
CZD-02/03	122	1343.9	11.0	532.9	768.0	53.6	2.8

conditions (MEI = −0.11 and 0.86, respectively). In addition to the MEI, spatial patterns in the sea surface temperatures (SST) further illustrate the ENSO differences between these years. Composite SST analyses were derived from the coarse (~2.5° latitude × ~2.5° longitude) daily global gridded dataset from the National Centers for Environmental Prediction–National Center for Atmospheric Research (NCEP–NCAR) reanalysis project (Kalnay et al. 1996). Composite SST mean and anomaly[2] fields were constructed for the 3-month period January–March for 1998, 2001, 2002, and 2003 (Fig. 7). The CALJET winter of 1998 experi-

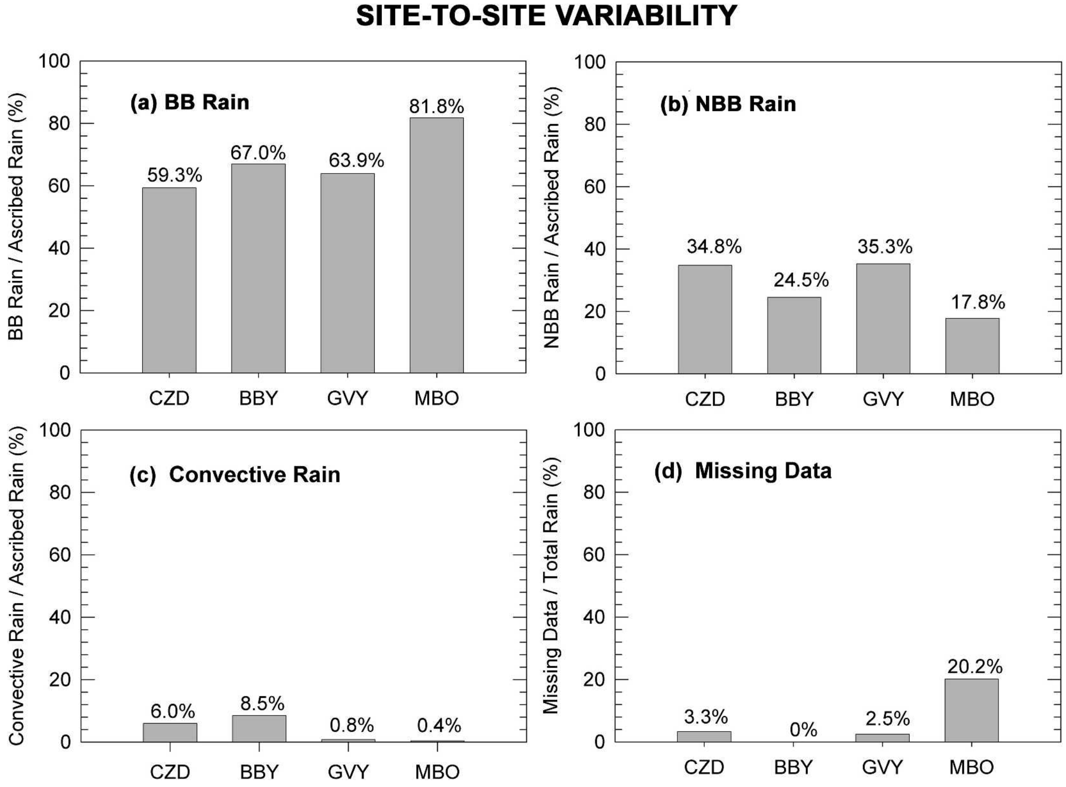

FIG. 5. The percent of total ascribed rainfall observed at each of the four S-PROF radar sites for (a) BB rain, (b) NBB rain, and (c) convective rain. Rainfall is only ascribed to a particular rain type when at least two tips of the rain gauge bucket occur in each half-hour period. (d) The percent of missing rain data relative to the total measured rainfall at each of the four S-PROF radar sites. "Missing rain" is defined as rainfall that met the two-tip criterion but could not be ascribed to a specific rain type by the objective process-partitioning algorithm because of issues related to snow (see text). The observations recorded at CZD are means based on the four winter seasons of data shown in Fig. 6.

---

[2] Reanalysis anomalies presented in this paper are obtained by subtracting the composite mean fields composed of specified dates from the long-term (1968–96) averages based on those same dates.

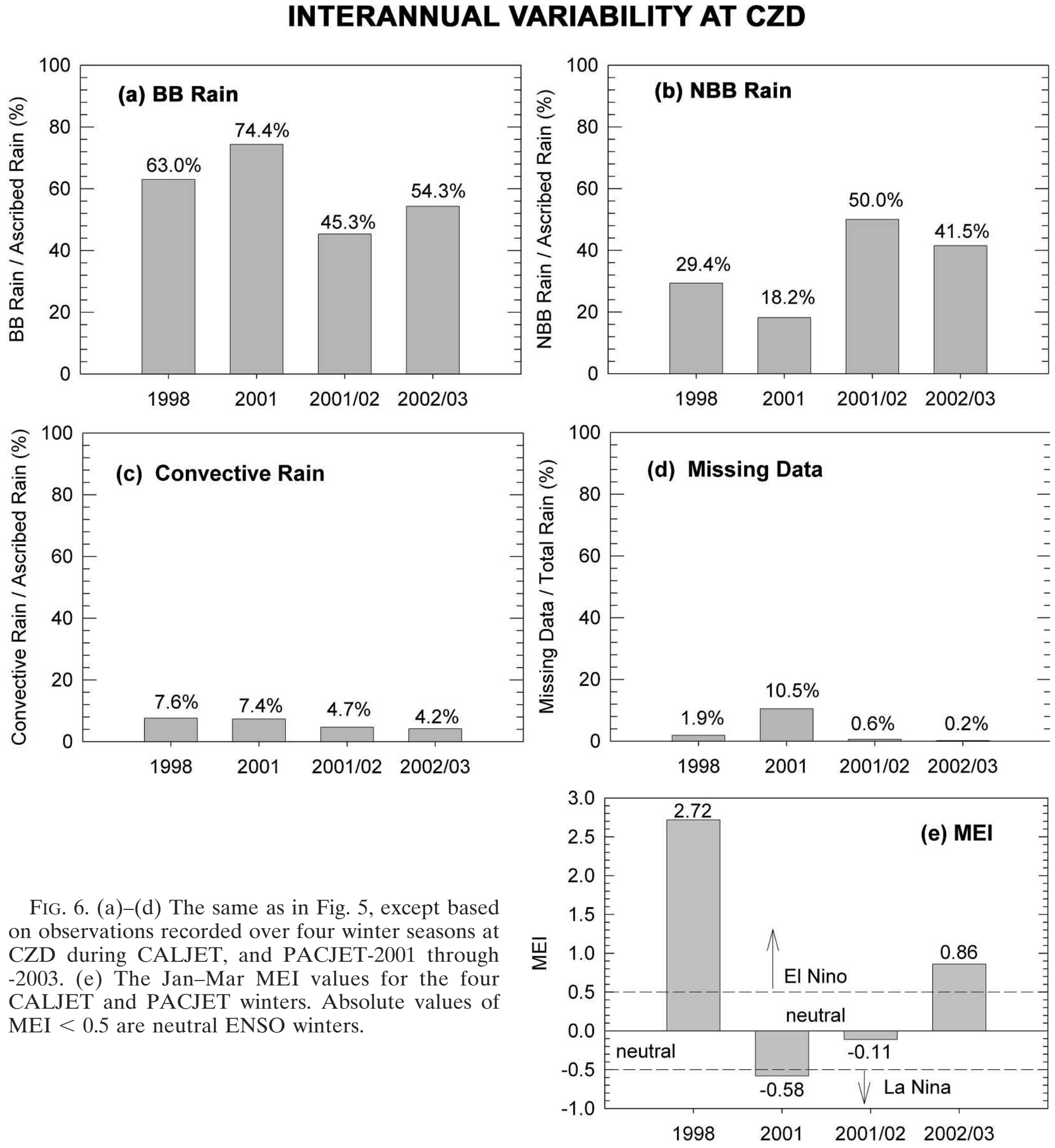

FIG. 6. (a)–(d) The same as in Fig. 5, except based on observations recorded over four winter seasons at CZD during CALJET, and PACJET-2001 through -2003. (e) The Jan–Mar MEI values for the four CALJET and PACJET winters. Absolute values of MEI < 0.5 are neutral ENSO winters.

enced anomalously warm (1°–3°C) SSTs in the equatorial eastern Pacific and along the west coast of North America. In contrast, the PACJET-2001 winter was characterized by weaker negative anomalies ($\leq -1.5°$C) in these same areas. Modestly weak negative and positive SST anomalies were observed offshore of California during PACJET-2002 and -2003, respectively.

NBB rain at CZD accounted for as little as 18% of the seasonal ascribed rainfall during the La Niña winter to as much as 50% in the neutral winter (Fig. 6b). The strong El Niño winter during CALJET received nearly 30% of its rain without a bright band, which is similar to the four-winter average. Clearly, NBB rain was significant in all four winters, and the single El Niño winter examined by White et al. (2003) was not unusual in this respect. Brightband rain dominated the winter-season rainfall (Fig. 6a) except during the neutral ENSO winter, while convection represented a small minority of total rainfall each winter (Fig. 6c). By far, the greatest percentage of missing data occurred in 2001 (Fig. 6d) because of snow-related issues during this unusually cold winter (see below).

The large-scale conditions responsible for generating significant rainfall at CZD during these four winters with distinctly different NBB percentages were gauged by constructing composite synoptic-scale analyses at 925 and 500 mb (Figs. 8 and 9) using the NCEP–NCAR reanalysis dataset. For each significant daily rain event measured at CZD during CALJET (defined as ≥12.5 mm total rainfall during a 0000–0000 UTC period), NCEP–NCAR's daily gridded data for the day of the rain event were included in the composites. An analo-

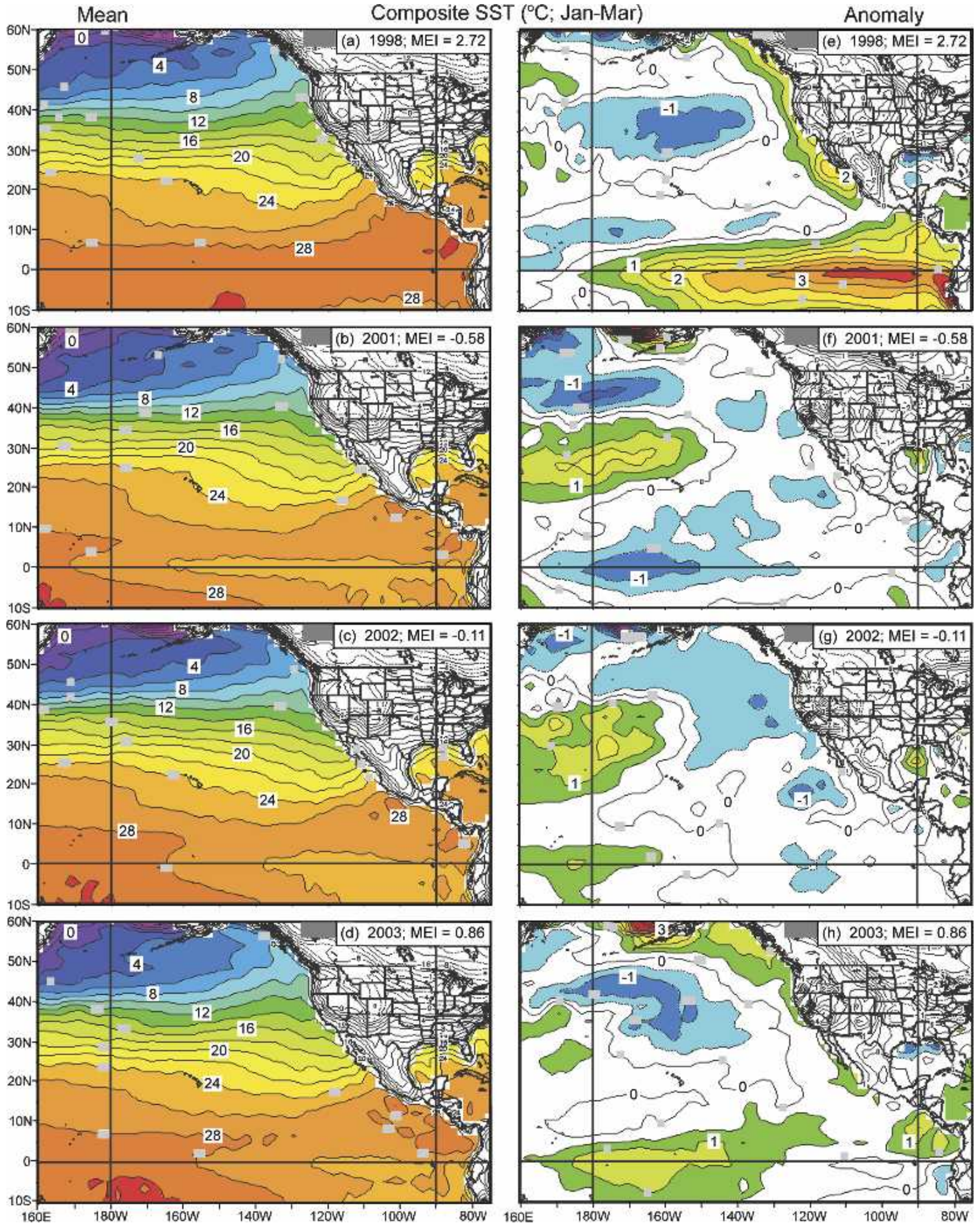

FIG. 7. Composite SST analyses (°C) for the 3-month Jan–Mar period derived from the NCEP–NCAR daily reanalysis global gridded dataset: SST means for (a) CALJET, (b) PACJET-2001, (c) PACJET-2002, and (d) PACJET-2003, and SST anomalies for (e) CALJET, (f) PACJET-2001, (g) PACJET-2002, and (h) PACJET-2003. The 3-month MEI values are shown in each panel.

gous set of composites was generated for PACJET-2001, -2003, and -2003. A total of 33, 17, 21, and 19 events were used in these composites. To further define the synoptic conditions associated with significant rain events at CZD for each of these years, mean low-level frontal positions derived from distinct features in the composite 925-mb thermal and water-vapor specific-humidity fields (not shown) are displayed in Fig. 8.

The mean storm characteristics responsible for significant rain events at CZD during the NBB-sparse La Niña winter of 2001 are strikingly different than those for the winters of 1998, 2002, and 2003 when much

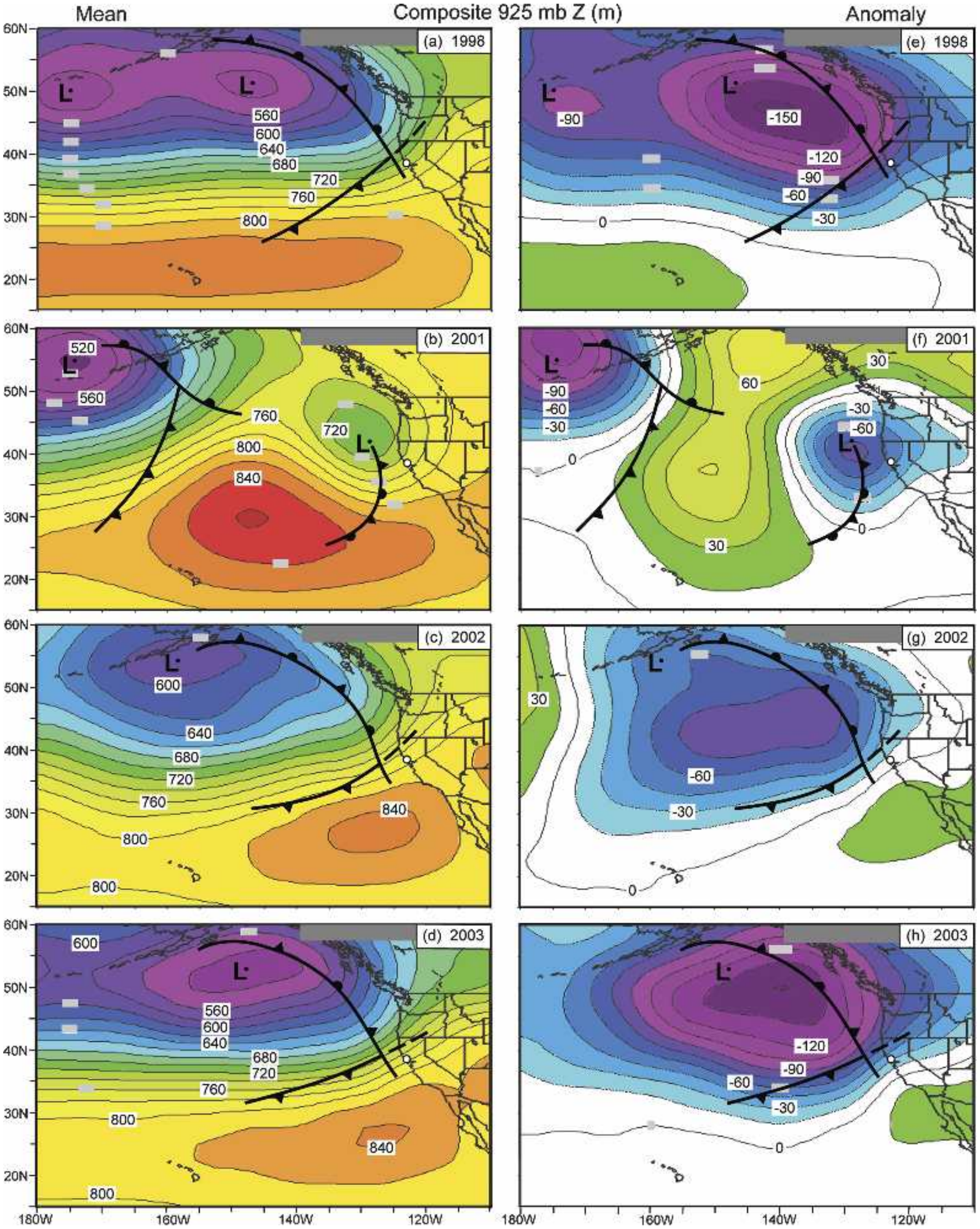

FIG. 8. Composite synoptic-scale 925-mb geopotential height (Z) analyses (m) derived from the NCEP–NCAR daily reanalysis global gridded dataset for daily rain events (i.e., from 0000 to 0000 UTC) at CZD (bold white dot) that exceeded 12.5 mm: means for (a) CALJET, (b) PACJET-2001, (c) PACJET-2002, and (d) PACJET-2003, and anomalies for (e) CALJET, (f) PACJET-2001, (g) PACJET-2002, and (h) PACJET-2003. Standard frontal notation is used to mark the composite frontal positions. The bold dashed frontal lines mark the approximate positions of the polar cold front above the occlusion.

larger fractions of NBB rain were observed. Composite 925-mb geopotential height analyses (Fig. 8) for the three similar winters portray a deeply occluded cyclone and negative height anomalies (90–180 m) extending eastward from the Aleutian Islands to the Pacific Northwest that directed a long west-southwesterly fetch from the relatively warm central Pacific into California. A polar cold front extended northeastward from the open ocean to the coast-parallel occlusion that quite likely developed partly because of terrain effects (Berg-

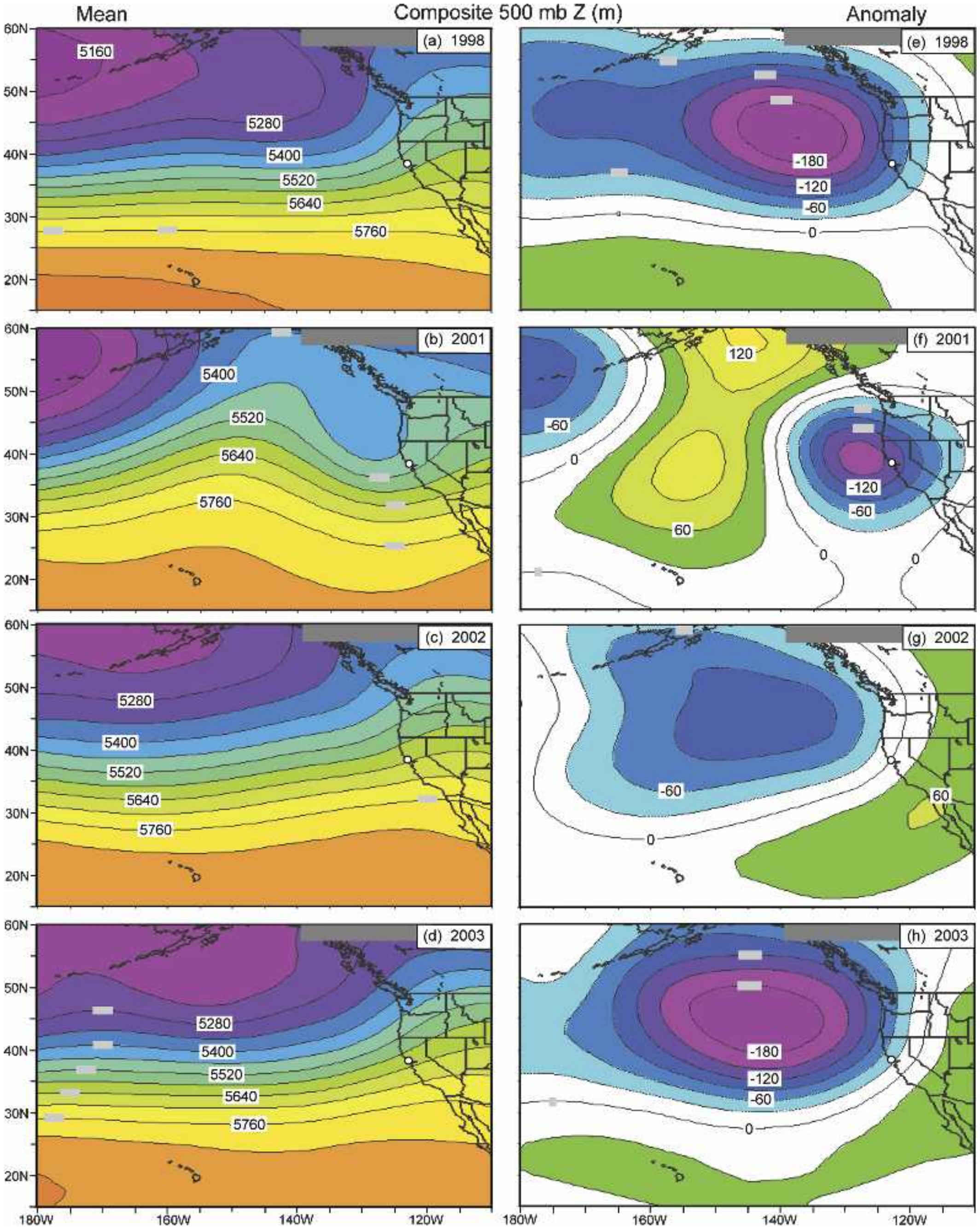

FIG. 9. The same as in Fig. 8, except for 500-mb geopotential height (Z; m).

eron 1937). East of the occlusion, the cold front aloft was situated north of CZD such that the mean conditions responsible for significant rainfall at CZD were tied to the pre-cold-frontal environment. In contrast, a cutoff cyclone offshore of the California–Oregon border during PACJET-2001 resulted in a short southwesterly ocean fetch into California. Aloft, the composite 500-mb geopotential height analyses (Fig. 9) for the similar winters exhibited low-latitude, quasi-zonal flow from the central Pacific into California. Negative height anomalies at 500 mb (100–200 m) spanned the eastern Pacific south of the Gulf of Alaska, while diffluent southwesterly flow aloft resided over CZD immediately downstream of a broad short-wave trough axis. In contrast, 500-mb ridging over the eastern Pacific during PACJET-2001 produced northwesterly flow downstream of the ridge and upstream of a sharp trough axis offshore of California, although CZD was again be-

TABLE 3. Winter-season S-PROF observations at CZD of the percentage of total ascribed rain attributed to NBB conditions and the mean brightband height, and the 500-mb geopotential height (mean and anomaly) and 925–700-mb layer-mean temperature at CZD based on composite synoptic-scale temperature analyses derived from the NCEP–NCAR daily reanalysis global gridded dataset for daily rain events that exceeded 12.5 mm.

	S-PROF observations at CZD		Composite synoptic-scale values at CZD	
Year	Fraction of total rain attributed to NBB conditions (%)	Mean brightband height (km, MSL)[a]	500-mb geopotential height mean/anomaly (m)[c]	925–700-mb layer-mean temperature (°C)
1998	29.4	1.79[b]	5550/−82	2.2
2001	18.2	1.24	5499/−139	−1.1
2001/02	50.0	2.14	5631/0	3.1
2002/03	41.5	1.91	5617/−38	2.9

[a] Based on the results of a statistical analysis technique that yielded contoured frequency-by-altitude diagrams described at the beginning of section 4b.

[b] This value is 20 m lower than that reported in White et al. (2003) because ~2% of the heaviest BB rainfall was removed in that study.

[c] These values were extracted from Fig. 9.

neath diffluent southwesterly flow. Composite thermodynamic analyses (not shown) reveal that the singular character of the 2001 winter was a manifestation of unusually cold conditions over California and Oregon. The collection of analyses suggests that the storms impacting CZD during the NBB-sparse winter originated from more northerly locations with different synoptic-scale airmass attributes than storms during the three other winters.

Additional systematic differences in the composite 500-mb analyses may help explain further the interannual variability of NBB rain at CZD. Specifically, a direct relationship exists between the fraction of winter-season NBB rain observed at CZD and the magnitude of the 500-mb geopotential height means and anomalies at that site (Table 3). This result implies that storms that are stronger and/or closer to CZD produce a lesser fraction of NBB rain than storms that are weaker and/or more distant. A direct relationship also exists between the fraction of winter-season NBB rain observed at CZD and the magnitude of the composite synoptic-scale 925–700-mb layer-mean temperature at that site (Table 3); namely, warmer lower-tropospheric conditions are more conducive to the formation of NBB rain. Observations of the mean winter-season brightband height at CZD, which can be considered a proxy for mean lower-tropospheric temperature, also correlate directly with the fractional occurrence of NBB rain (Table 3). The relationship between mean synoptic conditions and the occurrence of NBB and BB rain is the focus of the following subsection.

b. *Stratification by rain type: NBB versus BB rain*

The distinctly different bulk microphysical properties of BB and NBB rain observed at CZD during the four winters are highlighted statistically using contoured frequency-by-altitude diagrams (CFADs; Yuter and Houze 1995). The methodology used to produce the CFADs in Fig. 10 is the same as in White et al. (2003), with the following exceptions: 1) the ~2% of the heaviest BB rainfall was not excluded, since there was no attempt made to match the BB and NBB rain rates; 2) only every third radar profile from the BB and NBB half-hour periods during the 2001–2003 winters was included in the CFADs, thus ensuring roughly equal weighting from each year (i.e., the radar dwell times were ~3 times faster than during CALJET; Table 1); and 3) the 105-m-vertical-resolution profiles from CALJET were interpolated onto a 60-m grid, so that they could be combined with the 60-m-resolution profiles from the three other years. A total of 9825 and 7207 profiles were included in the BB and NBB CFADs, respectively. The multiwinter CFADs were similar to those observed during CALJET (White et al. 2003). For example, the BB CFADs (Figs. 10a,b) exhibited a rapid increase in DVV at the base of a prominent bright band at 1.81 km MSL and nearly constant values of DVV and reflectivity beneath, whereas the NBB counterparts (Figs. 10d, e) showed an increase in reflectivity and DVV with decreasing height below ~2.5 km. In addition, the reflectivities and DVVs (as defined by the axis of maximum frequency) were larger for BB than NBB rain across all altitudes. However, unlike during CALJET, the mean NBB rain rate for the four winters (3.07 mm h^{-1}) was appreciably smaller than the BB rain rate (4.22 mm h^{-1}), because the 4-yr NBB sample was composed of a smaller percentage of heavy rain events than for the CALJET NBB sample. Although it is not possible from Fig. 10 to infer that the mean drop sizes for NBB rain were smaller than for BB rain, it is reasonable to assume this, based on the results of White et al. (2003).

1) NCEP–NCAR SYNOPTIC-SCALE COMPOSITES

To explore the connection between the bulk microphysical properties of rainfall and mean synoptic conditions, the four winters of S-PROF data at CZD were stratified into two classes of significant daily rain events (defined as ≥12.5 mm of total ascribed rainfall during a 0000–0000 UTC period): those dominated by BB and NBB rain. The 32-case BB inventory (Table 4) is composed of daily rain events with ≥75% of the total ascribed rain accumulation tied to brightband conditions, and the 27-case NBB inventory (Table 5) contains daily

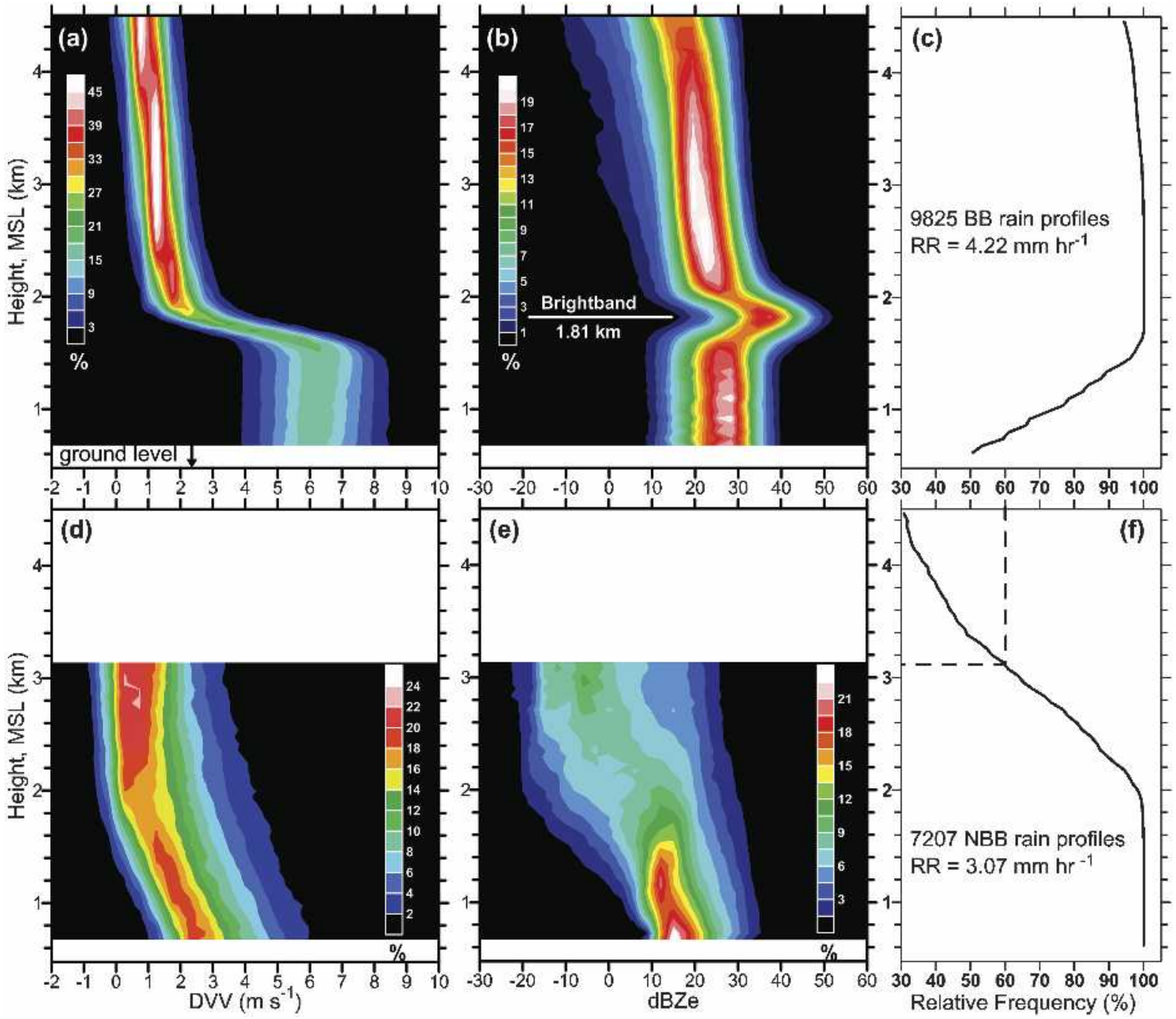

FIG. 10. CFADs produced from profiles of DVV (m s^{-1}) and equivalent radar reflectivity factor (dBZ_e) collected in rain with the S-PROF radar at CZD during CALJET and PACJET- through -2003: (a), (b) BB conditions and (d), (e) NBB conditions. The colored contours display the frequency of occurrence relative to the total number of observations available at a particular height. The DVV bin size is 0.5 m s^{-1} and the radar reflectivity bin size is 3 dBZ_e. The height of each BB rain profile was adjusted in 60-m increments so that the bright band occurred at the range-gate height closest to the average brightband height for the four winter seasons. No height adjustments were made for the NBB profiles. (c), (f) The percentage of profiles available at each range gate relative to the total number of profiles listed for BB rain and NBB rain, respectively. The NBB CFADs are shown for all range gates where the relative frequency exceeds 60%.

rain events with at least half of the ascribed totals attributable to nonbrightband, nonconvective conditions. NBB-dominated rain events were less common than their BB counterparts, so a less restrictive threshold of 50% was used to ensure that a sufficient number of NBB cases were considered. A total of 1223 mm (784 mm) of BB (NBB) rain fell during the BB- (NBB-) dominated events and accounted for 88% (72%) of the total ascribed rainfall. Because the process-partitioning algorithm ascribes a rain type with as few as 50% of the individual S-PROF profiles possessing or lacking a bright band in a given half-hour period, the average of the BB (NBB) rain events in Table 4 (Table 5) could conceivably be composed of a minority of BB (NBB) rain, given the 75% (50%) rain-event threshold employed. Consequently, we inspected the individual profiles contained within each half-hour period that were tagged as either BB or NBB rain to determine if these inventories were indeed dominated by their respective rain types. This "cross-check" (described in Tables 4 and 5) showed similar percentages of BB and NBB rain.

The large-scale conditions responsible for generating significant BB and NBB rain events were gauged by constructing NCEP–NCAR composite synoptic analy-

TABLE 4. Case inventory of daily rain events at Cazadero, CA, that exceeded 12.5 mm of ascribed rainfall, and at least 75% of the daily ascribed rainfall was associated with brightband conditions.

Date (MMDDYY)	Total rainfall (mm)	Total ascribed rainfall (mm)	Brightband rainfall		Nonbrightband rainfall		Convective rainfall	
			(mm)	%	(mm)	%	(mm)	%
011898[a]	57.9	57.9	48.7	84	5.1	09	4.1	07
012998[a]	56.4	54.3	43.9	81	10.4	19	0.0	00
020198[a]	42.2	42.2	32.0	76	10.2	24	0.0	00
020298[a]	26.9	26.2	26.2	100	0.0	00	0.0	00
020398[a]	58.4	58.1	52.0	89	6.1	10	0.0	00
020598[a]	138.9	120.4	100.8	84	1.3	01	18.3	15
020698[a]	99.1	98.3	78.5	80	7.4	07	12.4	13
020798[a]	52.6	50.8	38.3	75	12.4	25	0.0	00
021298[a]	20.3	18.8	14.0	75	4.8	25	0.0	00
021698[a]	39.9	39.6	36.8	93	1.0	03	1.8	04
021998[a]	116.1	115.1	109.3	95	0.0	00	5.8	05
022398[a]	35.1	34.0	34.0	100	0.0	00	0.0	00
031298[a]	23.6	22.6	22.6	100	0.0	00	0.0	00
031398[a]	19.8	18.5	15.2	82	3.3	18	0.0	00
032298[a]	36.3	33.8	27.7	82	6.1	18	0.0	00
012401[a]	27.2	26.7	23.1	87	3.6	13	0.0	00
012501[a]	54.4	46.2	35.3	76	7.9	17	3.0	07
012601[a]	23.9	16.8	16.3	97	0.5	03	0.0	00
020901[a]	28.2	26.9	24.4	90	1.5	06	1.0	04
021101[a]	19.3	15.2	15.2	100	0.0	00	0.0	00
021901[a]	35.6	33.3	28.0	84	5.3	16	0.0	00
030401[a]	101.1	98.6	79.6	81	10.9	11	8.1	08
030501[a]	18.3	17.0	14.0	82	3.0	18	0.0	00
122801	24.4	22.1	18.8	85	3.3	15	0.0	00
123001	18.0	16.0	15.5	97	0.5	03	0.0	00
123101	30.7	29.5	22.4	76	5.8	20	1.3	04
021702[a]	23.9	23.1	23.1	100	0.0	00	0.0	00
121302[a]	151.4	150.1	118.6	79	31.5	21	0.0	00
121502[a]	40.4	39.4	38.4	97	1.0	03	0.0	00
123002[a]	26.7	23.6	22.1	94	1.5	06	0.0	00
021603[a]	39.4	38.6	35.6	92	0.0	00	3.0	08
040403	15.2	14.0	13.0	93	1.0	07	0.0	00
Total[b]	1501.6	1427.7	1223.4		145.4		58.8	
Mean 1[b]	46.9	44.6	38.2	88	4.6	10	1.8	2
Mean 2[c]				79		21		

[a] Dates when daily rain gauge data were also available from the nearby coastal site at BBY.

[b] Based on the rainfall totals in the table, which were obtained from the bulk half-hourly periods designated as either BB or NBB by the objective process-partitioning algorithm.

[c] Cross-check based on the 11 248 (2919) individual S-PROF profiles observed within the 475 (89) half-hourly rain periods designated as BB (NBB) by the objective process-partitioning algorithm. This cross-check assumes equal-intensity rain fell during the individual BB and NBB profiles in each half-hour period. The half-hourly periods that were subjectively flagged as "convection" were not considered.

ses using the dates in Tables 4 and 5. The composite 925-mb geopotential height analyses for both rain types (Fig. 11) portray a deeply occluded cyclone with large negative anomalies from the Aleutians to the Pacific Northwest and a quasi-zonal fetch from the central Pacific into California. However, the BB storm composites show considerably lower mean and anomaly values over CZD and a much deeper storm center to the northwest than the NBB composites. The difference between the 925-mb mean heights at CZD is statistically significant at a >99% confidence level, based on a two-sided *t* test (Mendenhall et al. 1981). Note that CZD was positioned in the composite polar-cold-frontal zone aloft (derived from composite low-level thermal and moisture fields; not shown) for BB conditions but in a pre-cold-frontal environment for NBB conditions.[3] The preferential positioning of shallow NBB rain ahead of the cold front is consistent with observations of shallow warm-sector precipitation clouds in Browning (1990). Companion composites of integrated water vapor (IWV) for each rain type (Fig. 12) depict a plume of high moisture content (i.e., an atmospheric river; Ralph et al. 2004) and associated positive IWV anomalies paralleling the polar cold front on its warm side directed into California. However, the moisture content in the plume was greater in the NBB composite, and the difference between these compos-

---

[3] The NBB storm of 23 March 1998 (Fig. 2) was the exception, because a majority of the NBB rain fell in terrain-blocked, post-cold-frontal conditions.

TABLE 5. Case inventory of daily rain events at Cazadero, CA, that exceeded 12.5 mm of ascribed rainfall, and at least 50% of the daily ascribed rainfall was associated with nonconvective, nonbrightband conditions.

Date (MMDDYY)	Total rainfall (mm)	Total ascribed rainfall (mm)	Brightband rainfall		Nonbrightband rainfall		Convective rainfall	
			(mm)	%	(mm)	%	(mm)	%
010298[a]	75.2	73.7	14.5	20	59.2	80	0.0	00
010398[a]	27.2	24.9	1.5	06	23.4	94	0.0	00
011098[a]	28.2	25.1	1.0	04	24.1	96	0.0	00
012398[a]	14.7	14.2	5.8	41	8.4	59	0.0	00
021098[a]	26.2	25.9	12.4	48	13.5	52	0.0	00
022198[a]	108.7	107.7	18.3	17	76.7	71	12.7	12
032398[a]	75.4	74.9	6.3	09	62.5	83	6.1	08
022101[a]	30.7	19.6	8.7	44	10.9	56	0.0	00
121701	36.8	35.6	16.0	45	19.6	55	0.0	00
122001	47.2	45.2	11.2	25	28.4	63	5.6	12
010102	23.1	21.8	10.6	49	11.2	51	0.0	00
010202	131.3	130.0	45.4	35	84.6	65	0.0	00
010502	35.6	34.3	15.2	44	19.1	56	0.0	00
020702[a]	17.3	15.5	0.5	03	15.0	97	0.0	00
020802[a]	20.3	20.1	8.4	42	11.7	58	0.0	00
021902[a]	35.3	33.3	9.9	30	23.4	70	0.0	00
022002[a]	18.5	16.8	0.0	00	16.8	100	0.0	00
030602[a]	21.3	17.0	5.1	30	11.9	70	0.0	00
031002[a]	34.8	34.5	12.4	36	22.1	64	0.0	00
032202[a]	25.7	25.4	12.2	48	13.2	52	0.0	00
122602[a]	36.1	33.5	10.4	31	23.1	69	0.0	00
122702[a]	60.5	58.7	14.0	24	44.7	76	0.0	00
011003[a]	29.0	25.7	5.7	22	18.5	72	1.5	06
011303[a]	58.4	57.4	3.3	06	54.1	94	0.0	00
012203[a]	50.8	47.8	11.5	24	36.3	76	0.0	00
012303[a]	14.2	13.7	0.0	00	13.7	100	0.0	00
031403[a]	51.6	50.5	12.7	25	37.8	75	0.0	00
Total[b]	1134.1	1082.8	273.0		783.9		25.9	
Mean 1[b]	42.0	40.1	10.1	26	29.0	72	1.0	2
Mean 2[c]				30		70		

[a] Dates when daily rain gauge data were also available from the nearby coastal site at BBY.

[b] Based on the rainfall totals in the table, which were obtained from the bulk half-hourly periods designated as either BB or NBB by the objective process-partitioning algorithm.

[c] Cross-check based on the 5851 (13 323) individual S-PROF profiles observed within the 131 (421) half-hourly rain periods designated as BB (NBB) by the objective process-partitioning algorithm. This cross-check assumes equal-intensity rain fell during the individual BB and NBB profiles in each half-hour period. The half-hourly periods that were subjectively flagged as "convection" were not considered.

ites at CZD is statistically significant with 95% confidence. The anomaly fields suggest a link to the tropical moisture reservoir only in the NBB composite, consistent with the fact that the 925-mb NBB composite geopotential mean (Fig. 11b) shows a closed anticyclone west of Baja with southerly-component geostrophic flow extending from Hawaii into the midlatitudes, whereas the BB counterpart (Fig. 11a) portrays a west–east-oriented ridge at ~23°N preventing the northward transport of moisture from the tropical eastern Pacific.

NCEP–NCAR mandatory-level composite analyses were used to construct thermodynamic profiles representing conditions in the vicinity of CZD during BB and NBB rain (Fig. 13). The potential temperature was warmer for NBB conditions (Fig. 13a), consistent with the interannual dependence of rain-type frequency on temperature (Table 3). The difference between these composites increased from ~1 K near the surface to nearly 4 K aloft, resulting in a composite melting-level height of 2.50 km for NBB rain versus 1.95 km for BB rain.[4] Although moisture content was uniformly greater for the NBB composite profile (Fig. 13b), the relative humidity for BB rain exceeded that for NBB rain above ~1.5 km MSL (Fig. 13c) because of the much larger heat content in the NBB profile aloft. Composite profiles of equivalent potential temperature for BB and NBB rain exhibited similar structure (Fig. 13d), although the NBB profile was 2–4 K warmer. Static stability was quantified from the composite thermodynamic profiles by calculating dry and moist Brunt–Väisälä frequencies (N_d^2 and N_m^2, respectively) based on the formulations by Durran and Klemp (1982). The composite N_d^2 profiles (Fig. 13e) reveal significantly greater dry stratification below ~3 km MSL in the NBB

---

[4] A 140-m offset exists between the composite melting-level height of 1.95 km for BB rain and the 4-yr mean BB height of 1.81 km observed by the S-PROF radar (Figs. 10a,b). This is consistent with the fact that snow typically exists up to several hundred meters below the melting level before changing phase completely.

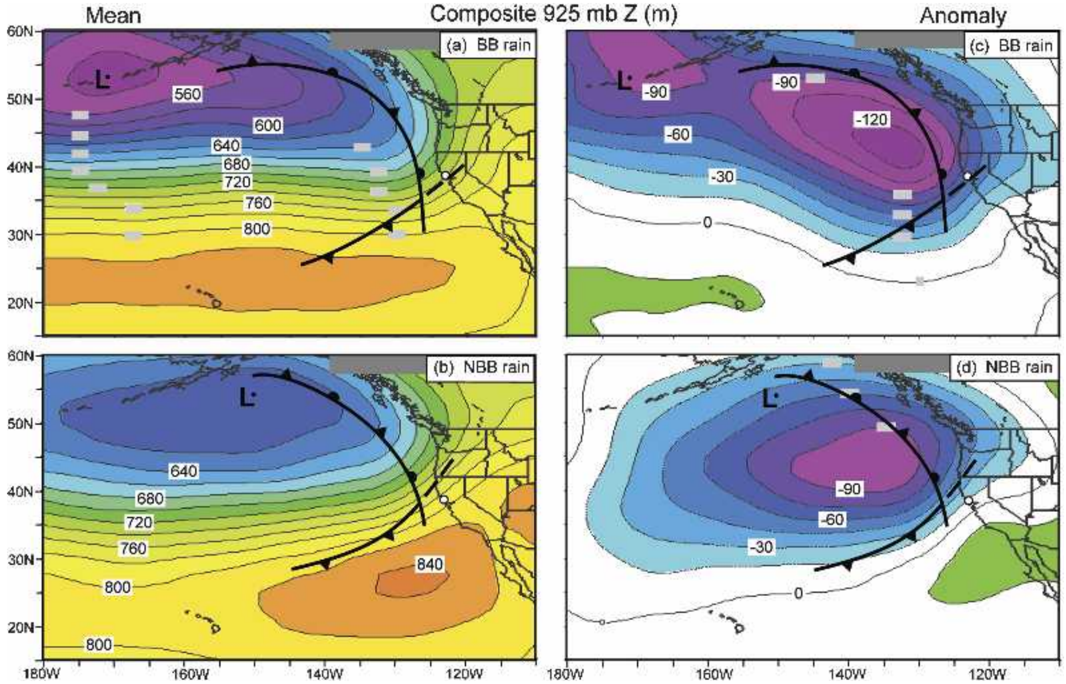

FIG. 11. Composite synoptic-scale mean 925-mb geopotential height (Z) analyses (m) derived from the NCEP–NCAR daily reanalysis global gridded dataset for significant daily rain events (i.e., from 0000 to 0000 UTC) at CZD (bold white dot) with (a) BB attributes and (b) NBB attributes. (c) and (d) The anomaly counterparts for (a) and (b), respectively. Fronts are as in Fig. 8.

regime. In contrast, the $N_m{}^2$ profiles (Fig. 13f) are quite similar, including the depiction of moist instability (i.e., potential instability, given $N_d^2 > 0\ \mathrm{s}^{-2}$) below the tops of the coastal mountains at ~1.5 km MSL. Hence, orographic rainfall enhancement should be expected when a saturated boundary layer impinges upon the coastal mountains, independent of rain type. This assertion is supported by observations from the CZD rain gauge

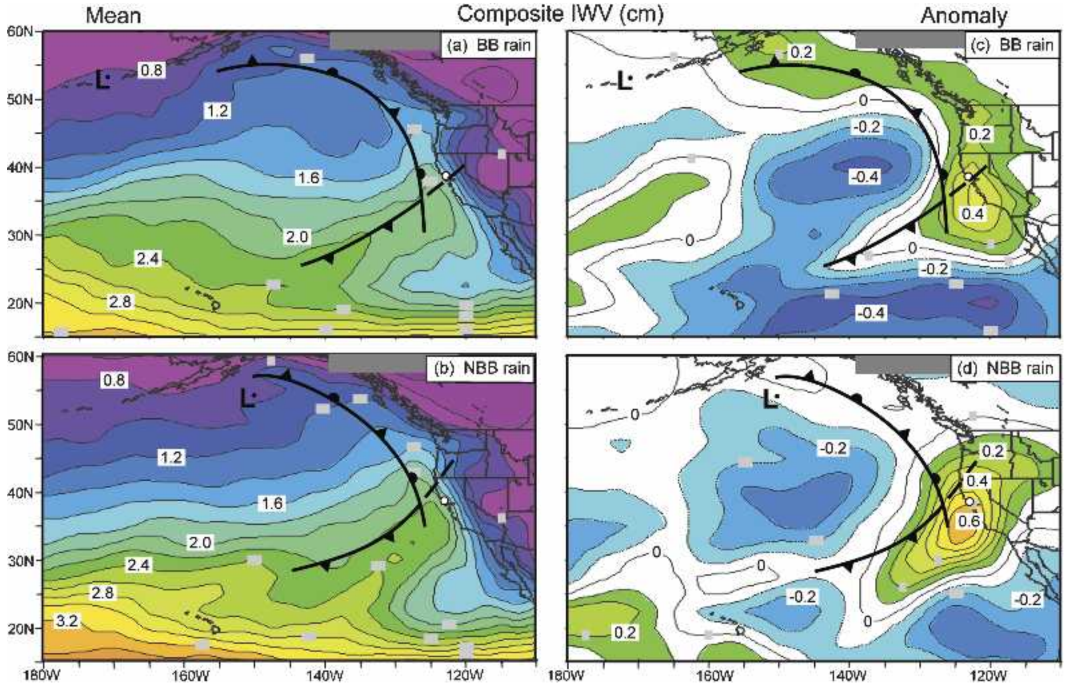

FIG. 12. The same as in Fig. 11, except for IWV (cm).

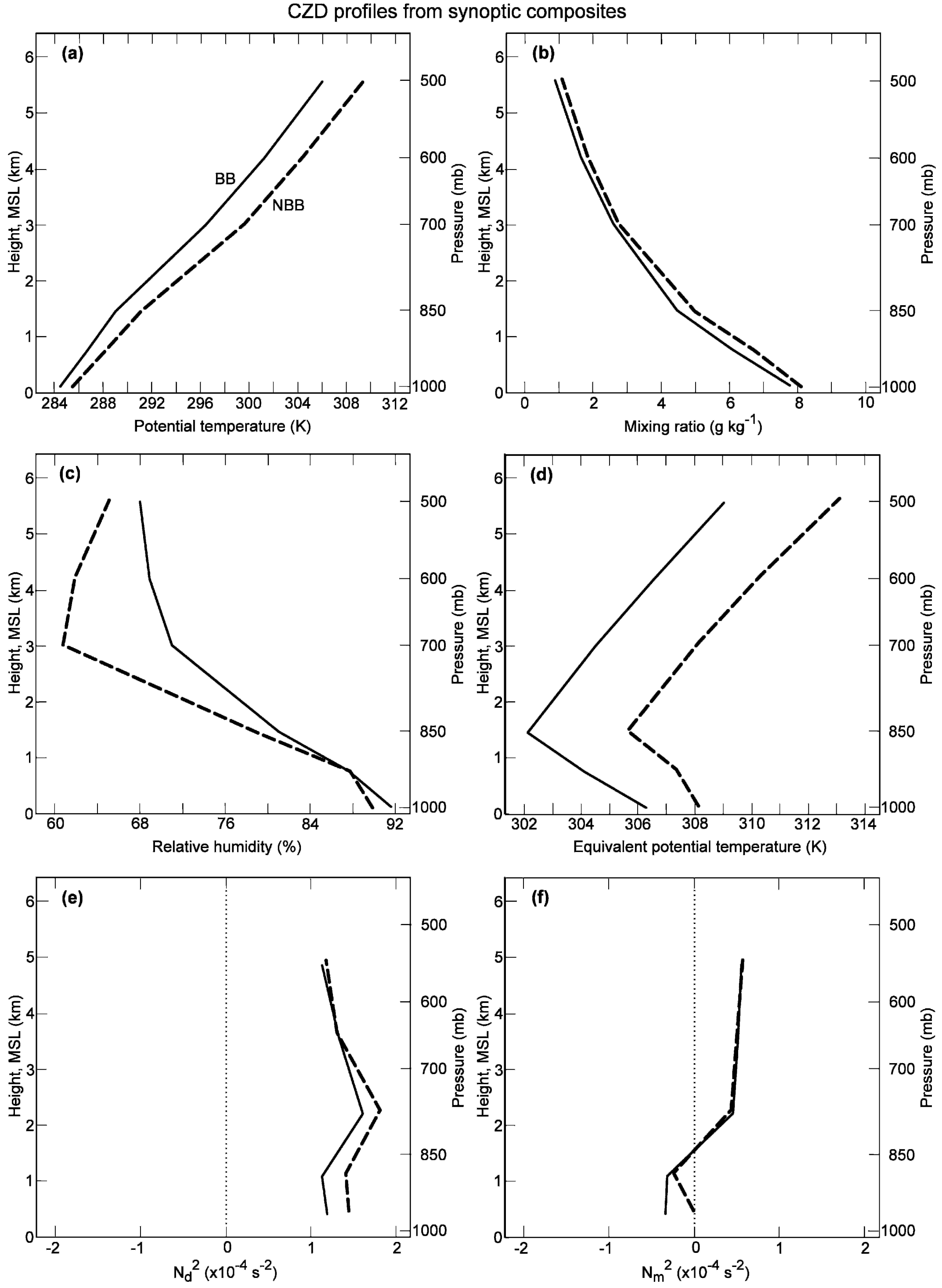

FIG. 13. Composite profiles representing conditions in the vicinity of CZD derived from the NCEP–NCAR daily reanalysis global gridded dataset for significant daily rain events (i.e., from 0000 to 0000 UTC) at CZD with BB (solid) and NBB (dashed) attributes: (a) potential temperature (K), (b) mixing ratio (g kg^{-1}), (c) relative humidity (%), and (d) equivalent potential temperature (K). (e), (f) Profiles of the square of the dry and moist Brunt–Väisälä frequency (N_d^2 and N_m^2, respectively; $\times 10^{-4}$ s^{-2}) derived from the profiles in (a)–(d).

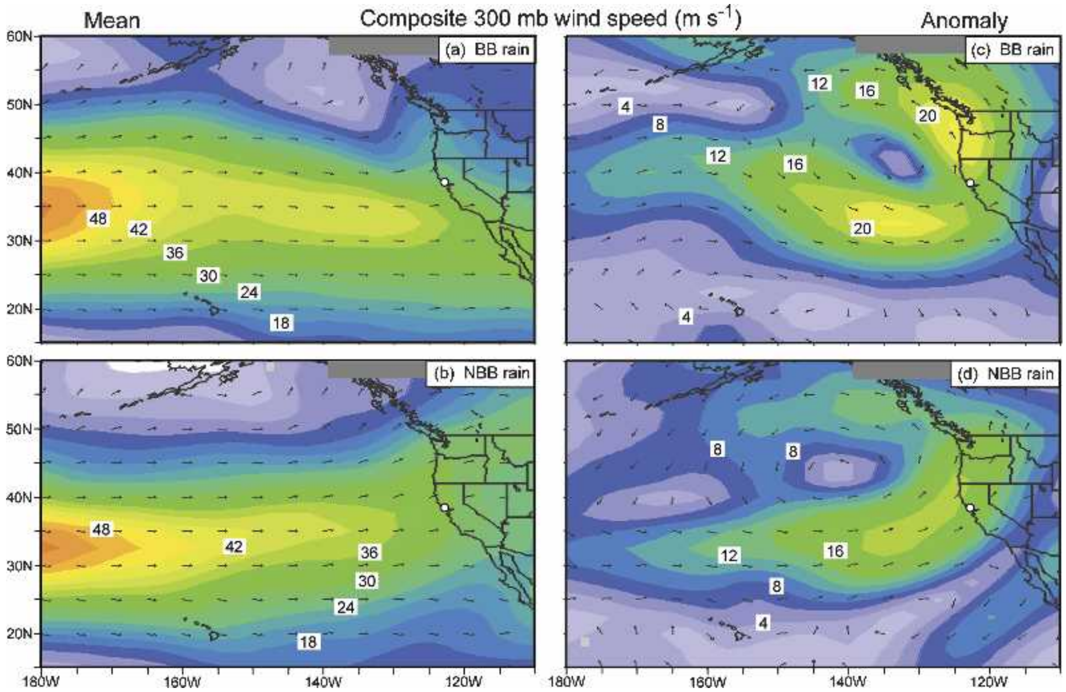

FIG. 14. The same as in Fig. 11, except for 300-mb wind speed (m s^{-1}).

and nearby coastal rain gauge at BBY; namely, the average rainfall ratios between these sites for BB and NBB rain are both much greater than unity (2.10:1 and 2.83:1, respectively; see Tables 4 and 5 for the dates used to calculate these ratios). The composite sounding results are analogous to the findings of Ralph et al. (2005), who revealed through an analysis of offshore dropsonde data that orographic rainfall enhancement was expected during two winters with very different ENSO and synoptic conditions (i.e., CALJET-1998 and PACJET-2001).

Additional synoptic composite analyses presented below further support the interannual results, which suggest that large-scale dynamical forcing impacts microphysical processes. For example, 300-mb wind speed analyses for each rain type (Fig. 14) show a quasi-linear jet stream directed from the central Pacific to the U.S. West Coast. Even though the magnitude of the wind speed at CZD is similar in these composites, the BB composite places CZD in the left exit region of the jet where large-scale deep ascent associated with a transverse circulation typically occurs, whereas the NBB composite depicts CZD near the often subsident right exit region (e.g., Keyser and Shapiro 1986). Companion 500-mb geopotential height analyses (Fig. 15) portray a sharper shortwave trough west of California for BB conditions and 90-m lower mean and anomaly values over CZD for this rain type (the mean difference is statistically significant with >99% confidence). This latter result mirrors the interannual findings that reveal a dependence of rain-type frequency on 500-mb heights at CZD (Table 3). Finally, the 925-mb analyses (Fig. 11) show CZD within the polar-cold-frontal zone in the BB composite but in the pre-cold-frontal regime for NBB rain. Alternately stated, frontal baroclinic forcing focused the upward motion at CZD during BB rainstorms, but this forcing was clearly well north of CZD in NBB events.

The analyses described above provide dynamically consistent evidence that synoptically forced ascent is stronger and deeper during BB than NBB rain at CZD. This link between dynamical forcing and rain type is quantified further by generating composite vertical-motion (ω) fields (Fig. 16) from the NCEP–NCAR reanalysis database. A prominent ascent maximum at 500 mb was centered over CZD for BB rain but displaced north of the site for NBB rain (Figs. 16a,b), reflecting the more northern placement of the polar cold front and upper-level jet for NBB conditions. A northward offset was also observed between the 925-mb ascent maxima (Figs. 16c,d). The ascent at CZD was ~60% larger at 500 mb for BB than NBB rain (with >99% confidence), but it was comparable in magnitude at 925 mb. Composite ω profiles in the vicinity of CZD (Fig. 16e) show classical synoptic-scale structure only for BB conditions. Namely, upward motion during BB rain attains its peak value at 600 mb (4 km MSL), which is near the climatological level of nondivergence for synoptic-scale weather systems (Carlson 1991). In contrast, the strongest ascent for NBB rain is confined to a lower altitude, thus implying that the dominant ω forcing mechanisms for NBB rain are vertically capped. Com-

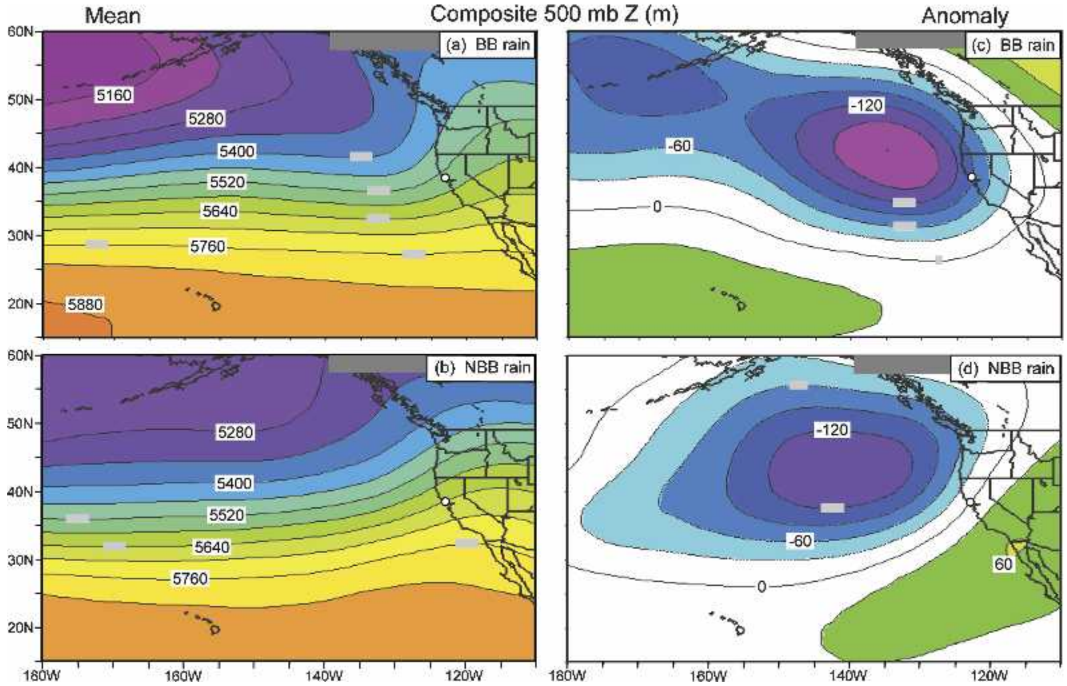

FIG. 15. The same as in Fig. 11, except for 500-mb geopotential height (*Z*; m).

paratively weak upward motion aloft for NBB rain, coupled with the fact that NBB conditions typically possess lower relative humidities aloft (Fig. 13c), suggests that NBB rain is associated with shallower cloud tops than BB rain. This has been shown in the case studies (Figs. 2–4) and will be highlighted further with a composite satellite analysis.

Clearly, weak and shallow synoptic-scale ascent contributed to the shallow character of NBB rain at CZD. But did physical processes other than weak synoptic-scale forcing contribute to the formation of NBB rain? Although the coarse-resolution reanalysis dataset cannot explicitly resolve mesoscale processes, the composite reanalysis soundings of Brunt–Väisälä frequency (Figs. 13e,f) reveal that mesoscale orographic forcing should occur during both rain types provided shallow upslope flow is present. In fact, composite reanalysis wind-velocity soundings at CZD for BB and NBB rain (not shown) reveal that upslope flow (defined as the component of the flow directed orthogonal to the local mountain barrier, i.e., directed from 230°; Neiman et al. 2002) was indeed present at and below 850 mb during both rain types, with a layer-mean value of 6.3 m s^{-1}. However, the upslope flow in this shallow layer was systematically stronger (by 1.1 m s^{-1}) for NBB rain, largely because the NBB wind-direction profile was rotated clockwise by ~10° relative to the more southerly BB profile. These results, combined with the fact that the low-level flow is warmer and moister with NBB rain, suggest that orographically forced rainfall is enhanced during NBB conditions, consistent with the single-winter results of White et al. (2003). The difference in the CZD/BBY rainfall ratios for BB and NBB rain (2.10:1 and 2.83:1, respectively) quite likely reflects the combined effects of weaker synoptic ascent and stronger orographic forcing during NBB rain.

Although the composite analyses for BB and NBB rain events show well-defined distinctions in synoptic-scale conditions for the two situations, recall that the bright band often appeared, faded, and reappeared on short time scales of a few hours or less within the same storm. This is evident in the S-PROF time–height images in Figs. 2–4, and, more so, in higher temporal resolution data from an X-band polarimetric radar operating at Ft. Ross, California (on the coast west of CZD) during the winters of 2003 and 2004 (not shown). Thus, the meteorological conditions that most often favor the formation of NBB rain do not exclude BB rain from occurring, and vice versa.

2) GOES SATELLITE COMPOSITES

A quantitative measure of cloud-top temperatures (CTTs) representing BB and NBB conditions was obtained by compositing IR satellite imagery from NOAA/ETL's GOES archive, which consists of 8-km-resolution digital images available every 3 h on a cylindrical equidistant grid. This archive was searched to identify all available imagery corresponding to the 32 BB and 27 NBB daily rain events listed in Tables 4 and 5. Images were extracted for all BB (NBB) cases where the rainfall records indicated that BB (NBB) rain occurred continuously for the hour before through the

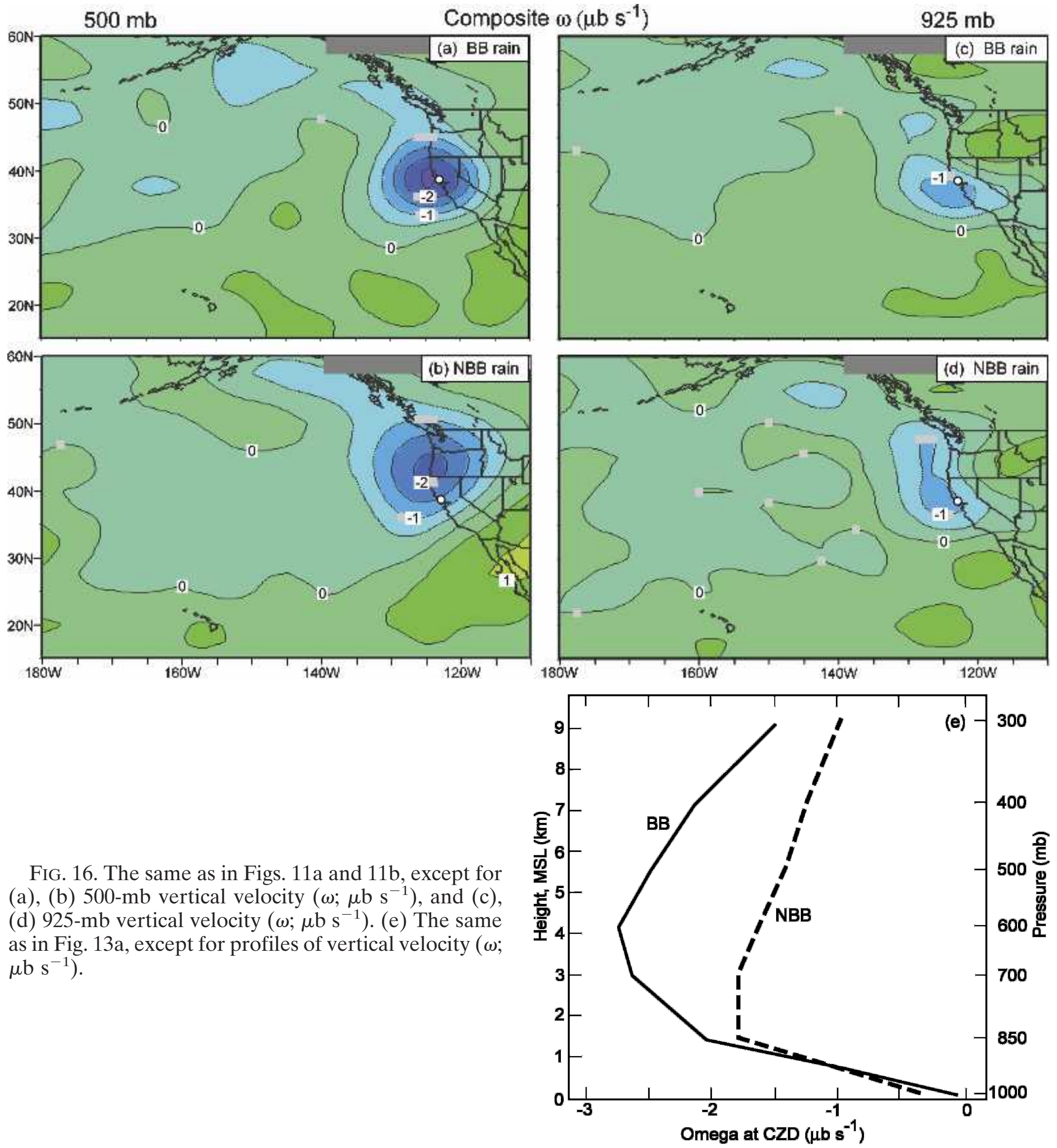

FIG. 16. The same as in Figs. 11a and 11b, except for (a), (b) 500-mb vertical velocity (ω; μb s^{-1}), and (c), (d) 925-mb vertical velocity (ω; μb s^{-1}). (e) The same as in Fig. 13a, except for profiles of vertical velocity (ω; μb s^{-1}).

hour after the image time. This step was taken to ensure that the satellite data were representative of the specified cases. Of the initial 32 BB and 27 NBB daily rain events considered, 33 satellite images from 22 days corresponded to the BB events and 28 images from 15 days were from the NBB events. If more than one image was available for a daily rain event, they were first averaged into a representative daily image before BB and NBB satellite composite images of CTT were generated (Fig. 17). This step assures that each daily BB and NBB rain event is given equal weighting in the respective composites. For each of the 61 images, the CTT over CZD was extracted by taking an average of the 3 × 3 array centered on that site. These values, as well as the 2-h rainfall flanking each image time, were used to construct the scatterplot in Fig. 18.

The composite IR images for BB and NBB rain (Fig. 17) possess distinct attributes that support the interpretations of the dynamical linkage between synoptic conditions and rain type. Namely, the coldest CTT was centered near CZD for BB rain but displaced northward over Oregon for NBB rain. In addition, the core region of enhanced CTT was colder for the BB composite. These contrasting images reflect the differing locations of the composite polar cold fronts and 300-mb jet streams, and the differing strengths of the composite 500-mb shortwave troughs offshore of California, for BB and NBB rain. The mean CTT over CZD was 231 and 251 K for BB and NBB rain, respectively, and this difference is statistically significant with >99% confidence. These CTTs correspond to cloud-top heights (CTHs) of 8.3 and 6.0 km MSL, assuming the synoptic

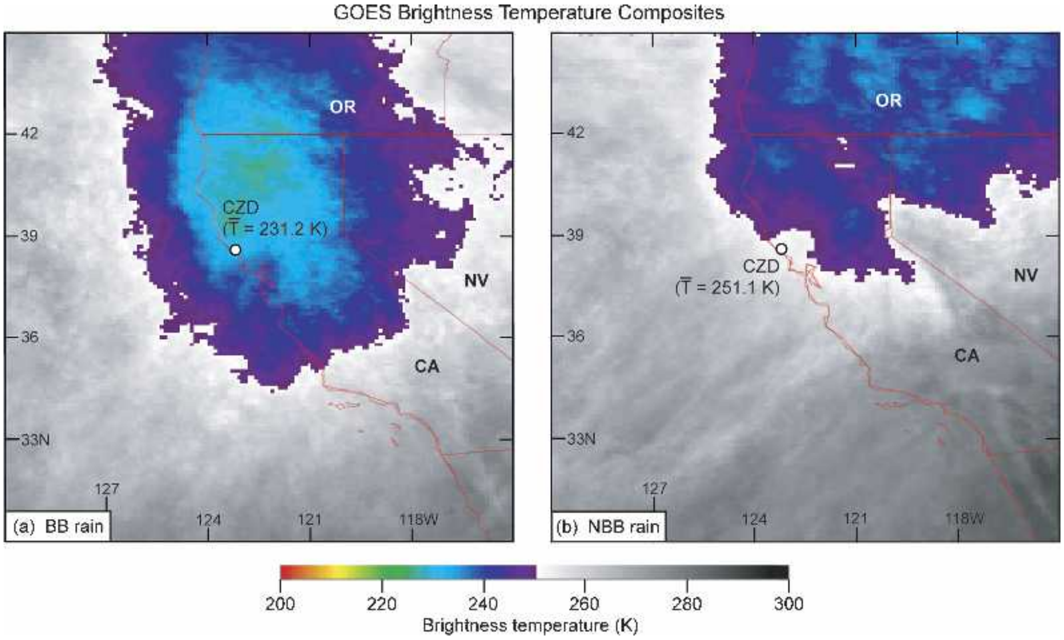

FIG. 17. GOES infrared satellite image composites of brightness (i.e., cloud top) temperature (K) based on significant daily rain events (i.e., from 0000 to 0000 UTC) at CZD (bold white dot) with (a) BB attributes and (b) NBB attributes. Images were included in the composites only when BB or NBB rain fell continuously for the hour before and after the image time. The mean cloud-top temperatures at CZD are shown.

composites used to obtain the CTHs accurately portrayed the thermodynamic conditions over CZD. The 20-K and 2.3-km differences in CTT and CTH are qualitatively consistent with the synoptic ω composites that show dynamically forced ascent over CZD to be much shallower and weaker for NBB conditions. Interestingly, a secondary region of enhanced cloud tops in the NBB composite (Fig. 17b) flanked CZD to its north and east and quite likely represents orographic clouds associated with forced lifting over the Sierra Nevada and Siskiyou Ranges. It is reasonable to assume that comparable orographic forcing also occurred during BB conditions over these areas, but cold cloud tops accompanying the BB rain events (e.g., Fig. 17a) would have prevented the satellite from viewing the orographic cloud enhancement beneath.

The scatterplot of CTT versus hourly rain rate for BB and NBB conditions at CZD (Fig. 18) reveals that the sample of NBB cases is generally warmer than the BB group, and the variability (i.e., standard deviation) of NBB points is about one-third greater than for BB rain. Significantly, none of the CTTs for BB rain at CZD is warmer than the CTT mean of 251.1 K for NBB conditions, and only one CTT corresponding to NBB rain is colder than the CTT mean of 231.2 K for BB conditions. CTTs associated with both rain types lie between the two means. Alternately stated, CTTs greater than ~250 K typically correspond to NBB events, while CTTs less than ~230 K are usually associated with BB events. At intermediate CTTs the rain types occur with similar frequency. It should be noted that CTTs associated with a majority of NBB rain events were sufficiently cold to support ice-phase precipitation aloft [based on observations in an orographic cloud over

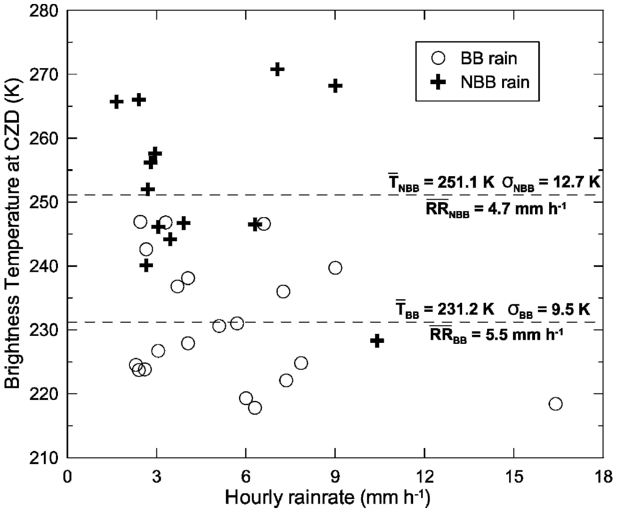

FIG. 18. Scatterplot of CZD brightness (i.e., cloud top) temperature (K) vs hourly rain rate (mm h^{-1}) for the BB and NBB daily rain events at CZD that were used to construct the satellite composites in Fig. 17. The dashed lines correspond to the mean cloud-top temperature at CZD for (lower line) BB and (upper line) NBB conditions. The standard deviation of cloud-top temperature at CZD and the corresponding mean hourly rain rate at CZD for BB and NBB conditions are also shown.

California's central Sierras by Rauber (1992)], which is consistent with our earlier statement that the formation of NBB rain does not exclude BB rain from occurring. Despite the 20-K difference in mean CTT at CZD for the two rain types, the rain rates are quite similar: 5.5 mm h^{-1} for BB rain versus 4.7 mm h^{-1} for NBB rain. Hence, wintertime NBB rainfall can be significant in California's coastal mountains when nearby cloud tops are relatively warm and low. However, because the correlation between CTT and rain rate for each rain type is quite small (i.e., ~0.07), CTT remains a poor predictor for rain intensity.

5. Conclusions

In an extension of an earlier study of NBB rain in California's coastal mountains at Cazadero (CZD) during the CALJET winter of 1998 (White et al. 2003), vertically pointing S-PROF radar data were examined from four geographically distinct locations in California and Oregon [i.e., California's coastal mountains (CZD) and nearby coastal plain (BBY); California's Sierra Nevada foothills (GVY); and Oregon's Cascades (MBO)] and from CZD for four winters (1998, 2001, 2001/02, 2002/03) to assess the geographic, interannual, and synoptic variability of NBB rain. The S-PROF data recorded during NBB-dominated rainstorms at CZD, GVY, and MBO highlight common temporal-vertical characteristics of NBB rain, independent of location. Most of the NBB rain that fell was light (<~5 mm h^{-1}), but it produced significant accumulations (23–62 mm) and occasionally yielded substantial rain rates (>12 mm h^{-1}) capable of generating flooding. The NBB rain fell in a shallow layer often residing beneath the melting level (<~3.5 km MSL), whereas BB rain was associated with much deeper echoes (>~6 km MSL). The quasi-steady character of the NBB rain implies that this rain type is nonconvective and possesses spatial uniformity, as was observed with airborne radar from the NOAA P-3 research aircraft during CALJET (White et al. 2003). NBB rain not only produced substantial accumulations during individual rainstorms, but it also contributed significantly to the total winter-season rainfall at these sites (as well as at BBY), despite the fact that BB rain accounted for a majority of the total. Specifically, 18% of the winter-season rainfall at MBO was ascribed to NBB conditions. This fractional value jumped to nearly 25% at BBY and to 35% at CZD (an average of four winter seasons) and GVY. These results demonstrate that NBB rain occurs with regularity in disparate geographic locations throughout the western United States.

The interannual variability of rain type at CZD was assessed based on four winters of S-PROF observations from that site. NBB conditions contributed significantly to the rainfall during these winters, which were characterized by different ENSO phases (MEI values ranging from 2.72 to −0.58 for strong El Niño to modest La Niña conditions, respectively), and the single El Niño winter examined by White et al. (2003) was not unusual in this respect. NBB rain accounted for as little as 18% of the seasonal accumulation during the La Niña winter of 2001 to as much as 50% in the near-neutral winter of 2001/02. The large-scale conditions responsible for generating significant daily rain events at CZD during these winters were gauged by constructing composite synoptic-scale analyses using NCEP–NCAR reanalysis data corresponding to the dates of those events. The composite analyses for each winter show a 500-mb shortwave trough and 925-mb polar cold front situated west of CZD. A direct trend exists between the fraction of winter-season NBB rain observed at CZD and the magnitude of the 500-mb geopotential height means and anomalies at that site. This result implies that storms that are stronger and/or closer to CZD produce a lesser fraction of NBB rain than storms that are weaker and/or more distant. A direct trend also exists between the fraction of winter-season NBB rain and the magnitude of the composite 925–700-mb layer-mean temperature at CZD; that is, NBB rain is more likely to occur in warmer lower-tropospheric conditions. Observations of the mean winter-season BB height at CZD, which can be considered a proxy for mean low-level temperature, also correlate directly with the fractional occurrence of NBB rain.

To showcase the large-scale conditions responsible for generating significant BB and NBB daily rain events at CZD during the four winters of S-PROF data collection, NCEP–NCAR composite synoptic analyses were created based on the reanalysis data for the 32 and 27 days during which significant BB and NBB rain events occurred. The composite analyses for both rain types portray a deeply occluded cyclone from the Aleutians to the Pacific Northwest and a quasi-zonal fetch from the central Pacific into California. The composites also reveal that synoptic conditions favoring BB rain exhibited notable distinctions from those characterizing NBB periods, as is summarized in a conceptual diagram (Figs. 19a,b). For BB periods the left exit region of the 300-mb jet stream and the underlying landfalling cold-frontal surface (i.e., features that typically favor focused synoptic-scale ascent) were located over CZD, whereas these features were situated north of CZD during NBB rain. Companion 500-mb composite height analyses portrayed a sharper shortwave trough west of California for BB conditions and ~90 m lower mean and anomaly values over CZD for this rain type. The relative humidity aloft over CZD was greater for BB rain, even though the moisture content was greater for NBB rain. And the synoptic vertical-motion composites over CZD showed stronger ascent distributed over a deeper layer for BB rain. Hence, the suite of BB composites exhibited dynamically consistent synoptic-scale characteristics that yielded more intense and deeper radar precipitation echoes over CZD than for NBB conditions (Fig. 19c). In essence, there appears to be a large-scale control of the microphysical processes. The composites also suggest that storms associated with NBB rain at CZD may preferentially tap into the tropical moisture reservoir (Figs. 19a,b). CZD was warmer and the melting level higher during NBB rain (by 1–4 K and 550 m, respectively; Fig. 19c), thus implying that the collision-coalescence process operates through a deeper layer than during BB rain. In addition, the fact that the radar reflectivity for NBB rain increases with decreasing height primarily beneath the melting level suggests that ice does not contribute significantly to this shallow rain type. Although NBB rain occurs in a more stably stratified environment, both regimes exhibit potential instability below the tops of the coastal mountains. Hence, orographic rain enhancement should be expected (and was observed) when a saturated boundary layer impinges upon these mountains, independent of rain type. The low-level upslope flow was stronger during NBB rain. This, combined with the fact that the low levels were warmer and moister during NBB rain, reveal that orographically forced rainfall should be enhanced during NBB conditions, an assertion borne out by local rainfall observations.

Composite IR satellite images for BB and NBB rainfall (Fig. 17) possess distinct attributes that support the interpretations of the dynamical linkage between synoptic conditions and rain type. Namely, the coldest CTT was centered near CZD for BB rain but displaced northward over Oregon for NBB rain. In addition, the core region of enhanced CTT was colder for the BB composite. The average cloud-top temperature at CZD was 251 K for NBB rain and 231 K for BB rain, corresponding to mean cloud-top heights of 6.0 and 8.3 km MSL, respectively. These cloud-top heights are shown in Fig. 19c and approximately match the uppermost radar reflectivity echo tops associated with the respective rain types. Despite the 2.3-km difference in cloud-top height between the two rain types, the rain rates associated with these satellite composites were similar: 5.5 mm h^{-1} for BB rain versus 4.7 mm h^{-1} for NBB rain. Hence, wintertime NBB rainfall can be significant in California's coastal mountains when nearby cloud tops are relatively warm and low. The elevated radar reflectivity maximum in the NBB profile (Fig. 19c) reveals that the composite NBB cloud top at 6 km is associated with a cloud layer that is decoupled (at least, in a mean sense) from the shallow NBB rain whose echo tops extend upward to only ~3 km MSL. Without

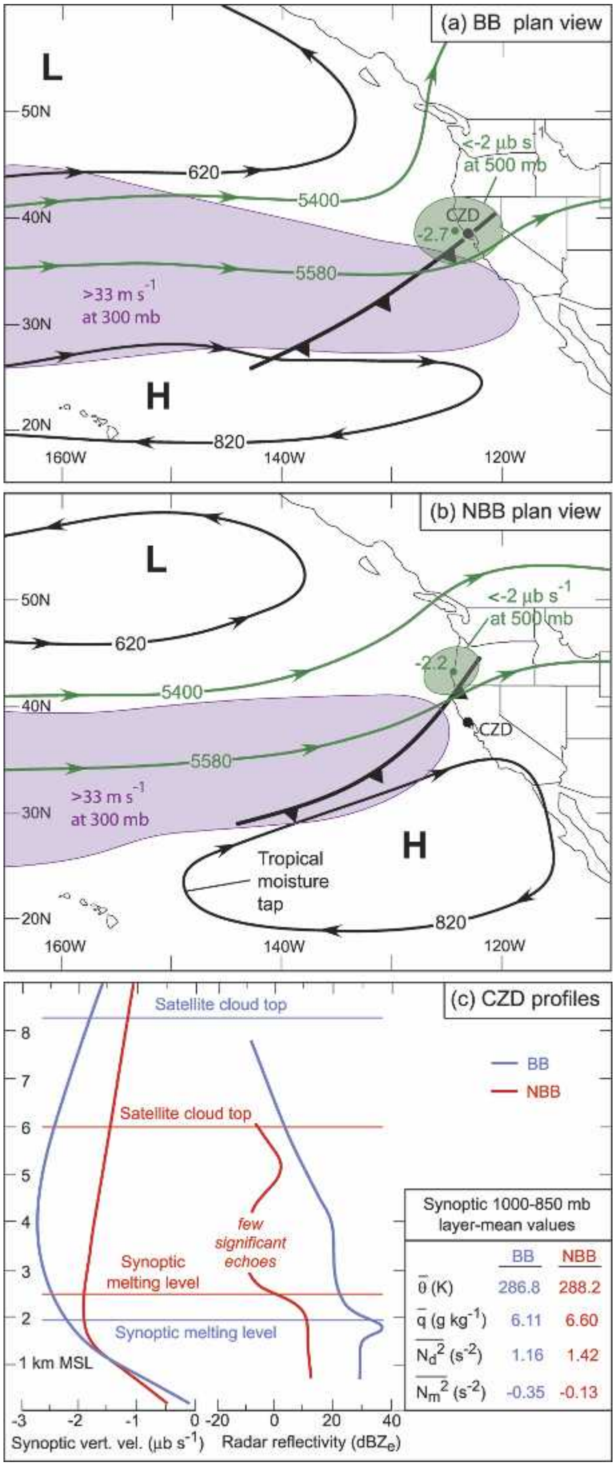

FIG. 19. Plan-view schematic of synoptic conditions associated with (a) BB and (b) NBB rain, at CZD. The black field corresponds to 925 mb [streamlines: geopotential height contours (m); frontal symbology: polar cold front], green denotes 500 mb [streamlines: geopotential height contours (m); shading: ascent stronger than −2.0 μb s^{-1}; bold dot: location of the strongest ascent, with value given], and purple is at 300 mb (shading: jet-stream flow >33 m s^{-1}). The 925-mb occluded front is excluded from each panel to simplify the presentation. (c) Profiles of synoptic-scale vertical velocity (μb s^{-1}; based on Fig. 16e) and S-PROF radar reflectivity (dBZ_e; modal profiles above the radar noise floor obtained from the CFAD analysis used to create Fig. 10) for BB and NBB rain (blue and red, respectively) at CZD. The altitudes of the synoptic-scale melting level and satellite-derived cloud-top height for each rain type are marked with thin, color-coded horizontal lines. The synoptic 1000–850-mb layer-mean values of key variables are shown in the lower right.

this decoupled cloud layer aloft, significant NBB rain can still occur (see Figs. 2–4).

The results of this study have important implications with respect to precipitation forecasting and nowcasting in the western United States, especially given that shallow NBB storm echo tops that are capable of producing flooding rains often reside beneath the coverage of the operational WSR-88Ds (White et al. 2003) and are poorly represented in GOES CTT products. Specifically, the synoptic conditions associated with NBB rain can be recognized in numerical model output by forecasters, and these forecasters can also consider the existing synoptic conditions when interpreting precipitation estimates from the WSR-88D and CTT observations from the GOES satellites. Clearly, NBB rain will challenge even multisensor quantitative precipitation estimation techniques from ground-based radars and space-based satellites. Finally, the origin (i.e., tropical versus midlatitude) of elongated moisture plumes or atmospheric rivers associated with landfalling cyclones can be considered when interpreting the local radar and regional GOES data. In summary, this newfound understanding of the linkage between synoptic conditions and rain type can be applied in practical terms by weather and river forecasters whose primary tasks include closely monitoring significant wintertime precipitation events affecting the western United States and warning the public of the potential adverse impacts of these events on personal safety, property, commerce, and transportation.

Acknowledgments. The successful implementation of the CALJET and PACJET programs was made possible by the dedicated participation of many individuals from numerous organizations. Special thanks are given to Clark King and the rest of NOAA/ETL's talented field and engineering teams for deploying and maintaining the instrumentation. The experimental data collection was supported, in part, by the U.S. Weather Research Program. Jessica Koury of ETL provided crucial assistance for the processing of the S-PROF data. GOES satellite data were supplied courtesy of NOAA/Forecast Systems Laboratory. Jim Adams furnished quality drafting services. We are grateful to the University of California, Davis, Bodega Marine Laboratory and to Robert Mann for granting us permission to deploy and operate ETL's instrumentation on a long-term basis at Bodega Bay and Cazadero, respectively. We appreciate the thoughtful input from Ola Persson of NOAA/ETL, Chris Williams of NOAA/AL, and two anonymous reviewers. Their efforts improved the scope and quality of this manuscript. This research was funded with the support of the Climate-Weather Connection Program in NOAA.

REFERENCES

Anagnostou, E. N., and C. Kummerow, 1997: Stratiform and convective classification of rainfall using SSM/I 85-GHz brightness temperature observations. *J. Atmos. Oceanic Technol.,* **14,** 570–575.

Battan, L. J., 1973: *Radar Observation of the Atmosphere*. University of Chicago Press, 324 pp.

Bergeron, T., 1937: On the physics of fronts. *Bull. Amer. Meteor. Soc.,* **18,** 265–275.

Blanchard, D. C., 1953: Raindrop size distributions in Hawaiian rains. *J. Meteor.,* **10,** 457–473.

Bond, N. A., and Coauthors, 1997: The Coastal Observation and Simulation with Topography (COAST) experiment. *Bull. Amer. Meteor. Soc.,* **78,** 1941–1955.

Browning, K. A., 1990: Organization of clouds and precipitation in extratropical cyclones. *Extratropical Cyclones: The Erik Palmén Memorial Volume*, C. W. Newton and E. Holopainen, Eds., Amer. Meteor. Soc., 129–153.

Carlson, T. N., 1991: *Mid-latitude Weather Systems*. HarperCollins, 507 pp.

Carter, D. A., K. S. Gage, W. L. Ecklund, W. M. Angevine, P. E. Johnston, A. C. Riddle, J. S. Wilson, and C. R. Williams, 1995: Developments in UHF lower tropospheric wind profiling at NOAA's Aeronomy Laboratory. *Radio Sci.,* **30,** 997–1001.

Cotton, W. R., and R. A. Anthes, 1989: *Storm and Cloud Dynamics*. Academic Press, 880 pp.

Durran, D. R., and J. B. Klemp, 1982: On the effects of moisture on the Brunt–Väisälä frequency. *J. Atmos. Sci.,* **39,** 2152–2158.

Fabry, F., and I. Zawadzki, 1995: Long-term radar observations of the melting layer of precipitation and their interpretation. *J. Atmos. Sci.,* **52,** 838–851.

Kalnay, E., and Coauthors, 1996: The NCEP/NCAR 40-Year Reanalysis Project. *Bull. Amer. Meteor. Soc.,* **77,** 437–471.

Keyser, D., and M. A. Shapiro, 1986: A review of the structure and dynamics of upper-level frontal zones. *Mon. Wea. Rev.,* **114,** 452–499.

Kummerow, C., J. Simpson, O. Thiele, W. Barnes, A. T. C. Chang, E. Stocker, R. F. Adler, and A. Hou, 2000: The status of the Tropical Rainfall Measuring Mission (TRMM) after two years in orbit. *J. Appl. Meteor.,* **39,** 1965–1982.

Maddox, R. A., J. Zang, J. J. Gourley, and K. W. Howard, 2002: Weather radar coverage over the contiguous United States. *Wea. Forecasting,* **17,** 927–934.

Matejka, T. J., R. A. Houze, and P. V. Hobbs, 1980: Microphysics and dynamics of clouds associated with mesoscale rainbands in extratropical cyclones. *Quart. J. Roy. Meteor. Soc.,* **106,** 29–56.

Mendenhall, W., R. L. Scheaffer, and D. D. Wackerly, 1981: *Mathematical Statistics with Applications*. 2d ed. Duxbury, 686 pp.

Neiman, P. J., F. M. Ralph, A. B. White, D. A. Kingsmill, and P. O. G. Persson, 2002: The statistical relationship between upslope flow and rainfall in California's coastal mountains: Observations during CALJET. *Mon. Wea. Rev.,* **130,** 1468–1492.

——, P. O. G. Persson, F. M. Ralph, D. P. Jorgensen, A. B. White, and D. E. Kingsmill, 2004: Modification of fronts and precipitation by coastal blocking during an intense landfalling winter storm in southern California: Observations during CALJET. *Mon. Wea. Rev.,* **132,** 242–273.

Ralph, F. M., P. J. Neiman, D. E. Kingsmill, P. O. G. Persson, A. B. White, E. T. Strem, E. D. Andrews, and R. C. Antweiler, 2003: The impact of a prominent rain shadow on flooding in California's Santa Cruz Mountains: A CALJET case study and sensitivity to the ENSO cycle. *J. Hydrometeor.,* **4,** 1243–1264.

——, ——, and G. A. Wick, 2004: Satellite and CALJET aircraft observations of atmospheric rivers over the eastern North Pacific Ocean during the winter of 1997/98. *Mon. Wea. Rev.,* **132,** 1721–1745.

——, ——, and R. Rotunno, 2005: Dropsonde observations in low-level jets over the northeastern Pacific Ocean from CALJET-1998 and PACJET-2001: Mean vertical-profile and atmospheric-river characteristics. *Mon. Wea. Rev.,* **133,** 889–910.

Rauber, R. M., 1992: Microphysical structure and evolution of a central Sierra Nevada orographic cloud system. *J. Appl. Meteor.,* **31,** 3–25.

Song, N., and J. Marwitz, 1989: A numerical study of the warm rain process in orographic clouds. *J. Atmos. Sci.,* **46,** 3479–3486.

Stoelinga, M. T., and Coauthors, 2003: Improvement of microphysical parameterization through observational verification experiment. *Bull. Amer. Meteor. Soc.,* **84,** 1807–1826.

Westrick, K. J., C. F. Mass, and B. A. Colle, 1999: The limitations of the WSR-88D radar network for quantitative precipitation measurement over the coastal western United States. *Bull. Amer. Meteor. Soc.,* **80,** 2289–2298.

White, A. B., J. R. Jordan, B. E. Martner, F. M. Ralph, and B. W. Bartram, 2000: Extending the dynamic range of an S-band radar for cloud and precipitation studies. *J. Atmos. Oceanic Technol.,* **17,** 1226–1234.

——, D. J. Gottas, E. T. Strem, F. M. Ralph, and P. J. Neiman, 2002: An automated brightband height detection algorithm for use with Doppler radar spectral moments. *J. Atmos. Oceanic Technol.,* **19,** 687–697.

——, P. J. Neiman, F. M. Ralph, D. E. Kingsmill, and P. O. G. Persson, 2003: Coastal orographic rainfall processes observed by radar during the California Land-Falling Jets Experiment. *J. Hydrometeor.,* **4,** 264–282.

Wolter, K., and M. S. Timlin, 1993: Monitoring ENSO in LOADS with a seasonally adjusted principal component index. *Proc. 17th Climate Diagnostics Workshop*, Norman, OK, NOAA/NMC/CAC, 52–57.

——, and ——, 1998: Measuring the strength of ENSO events: How does 1997/98 rank? *Weather,* **53,** 315–324.

Young, K. C., 1974: A numerical simulation of wintertime, orographic precipitation: Part I. Description of model microphysics and numerical techniques. *J. Atmos. Sci.,* **31,** 1735–1748.

Yuter, S. E., and R. A. Houze Jr., 1995: Three-dimensional kinematic and microphysical evolution of Florida cumulonimbus. Part II: Frequency distributions of vertical velocity, reflectivity, and differential reflectivity. *Mon. Wea. Rev.,* **123,** 1941–1963.

Zipser, E. J., and M. A. LeMone, 1980: Cumulonimbus vertical velocity events in GATE. Part II: Synthesis and model core structure. *J. Atmos. Sci.,* **37,** 2458–2469.